POLITECNICO DI MILANO
Corso di Laurea Magistrale in Ingegneria Aeronautica
Dipartimento di Scienze e Tecnologie Aerospaziali

A Numerical CFD Study to Support Clinical Tests of Graft-Gas Coverage after DMEK Eye Surgery

Relatore: Prof. Maurizio Quadrio
Correlatore: Prof. Jan O. Pralits

Tesi di Laurea di:
Víctor García Bennett
Matricola 912959

Anno Accademico 2019-2020

Socrates: And, if he compelled him to look at the light itself, would his eyes hurt and would he flee, turning away to those things that he is able to make out and hold them to be really clearer than what is being shown?

Republic (515e), Plato

Acknowledgements

A quelle notti sul 90

Abstract

In the current literature of Descemet's membrane endothelial keratoplasty (DMEK) little is known about the exact behaviour of the intraocular bubble in the post-operative period although it plays a crucial roll in the correct adherence and healing of the patient's graft. This Thesis has characterized said bubble, by taking as representative its projection on the cornea, using computational fluid dynamics. Its shape, size and position as well as the percentage of the donor's graft being covered have been totally described as a function of the patient's anterior chamber geometry, two-degree-of-freedom position and post-operative period, with a series of simple coefficients.

As an output of the research, the results are available in different forms for their clinical use. A priori formats such as contour graphs, time-averages and tables have been given to have insight about the consequences of certain decisions over the graft coverage after DMEK. A posteriori designs are also proposed such as heatmaps which can be utilized after the post-operative period to asses the quality of the treatment.

It has been shown that for small anterior chambers –especially in phakic eyes- the surgeon's ability to inject the correct amount of gas dominates over what the patient can do with his or her position. However, as the size of the anterior chamber increases -especially in pseudophakic eyes– the position of the patient gains importance. Although different post-operative scenarios have been studied, if the patient is lying down facing up s/he will achieve an almost optimal graft coverage. However, this compromise does not always yield a homogeneous gas contact over all the graft, hindering the bottom quadrants. To resolve this situation, the given optimal positioning should be pursued. Monitoring the position becomes more critical as the anterior chamber increases and for patients with pseudophakic eyes, while more relaxed measures could be applied to small -especially phakic- anterior chambers.

Keywords: DMEK, CFD, numerical model, intraocular bubble, intraocular gas, patient position, graft coverage, optimal position.

Sommario

Nell'attuale letteratura sulla *Descemet's membrane endothelial keratoplasty* (DMEK) poco si sa circa il comportamento esatto della bolla intraoculare nel periodo post-operatorio sebbene svolga un ruolo cruciale nella corretta aderenza e guarigione dell'innesto del paziente. Questa Tesi ha caratterizzato la bolla, prendendo come rappresentativa la sua proiezione sulla cornea, usando la fluidodinamica computazionale. La sua forma, dimensione e posizione, nonché la percentuale d'innesto del donatore coperto sono stati totalmente descritti come una funzione della geometria della camera anteriore del paziente, della posizione a due gradi di libertà e del periodo post-operatorio.

Come risultato della ricerca, i risultati sono disponibili in diverse forme per il loro uso clinico. Formati a priori come curve di livello, medie temporali e tabelle sono stati dati per avere un'idea delle conseguenze di alcune decisioni sulla copertura dell'innesto dopo DMEK. Sono anche proposti grafici a posteriori come le mappe di calore che possono essere utilizzate dopo il periodo post-operatorio per valutare la qualità del trattamento.

È stato dimostrato che per le piccole camere anteriori –specialmente negli occhi fachici– la capacità del chirurgo d'iniettare la corretta quantità di gas domina ciò che il paziente può fare con la propria posizione. Tuttavia, poiché la dimensione della camera anteriore aumenta –specialmente negli occhi pseudofachici, la posizione del paziente acquista importanza. Sebbene siano stati studiati diversi scenari post-operatori, se il paziente è sdraiato rivolto verso l'alto, otterrà una copertura dell'innesto quasi ottimale. Tuttavia, questo compromesso non sempre produce un contatto omogeneo del gas su tutto l'innesto, ignorando i quadranti inferiori. Per risolvere questa situazione, deve essere perseguito il posizionamento ottimale dato del paziente. Il monitoraggio della posizione diventa più critico con l'aumentare della profondità della camera anteriore e per i pazienti con occhi pseudofachici, mentre misure più rilassate potrebbero essere applicate a piccole -specialmente fachichecamere anteriori.

Parole chiave: DMEK, CFD, modello numerico, bolla intraoculare, gas intraoculare, posizione del paziente, copertura dell'innesto, posizione ottimale.

Contents

List of Figures

List of Tables

1 | Introduction

This Thesis has been conducted in collaboration with Prof. Jan O. Pralits[1] and Dr. Mark Alberti[2,3], as an extension of their current research, see Pralits et al. [1] and Alberti et al. [2]. In Appendix A a small discussion is given about the way this Thesis has been conducted and the organization of an international Master Degree Thesis (especially in times of SARS-CoV-2).

1.1 Motivation

This research will focus on the post-operative period of the Descemet's membrane endothelial keratoplasty (DMEK) medical procedure. During a DMEK surgery, the patient's Descemet's membrane and endothelium of the eye are removed and a graft –of about $10-15$ μm of thickness– is placed from a donor. After the donor's tissue is inserted, the surgeon unrolls the graft and orients it correctly. The adherence of the donor graft to the host cornea is done in a sutureless fashion. This procedure is followed by the injection of a gas (air or sulfur hexafluoride –SF6–) in the anterior chamber, AC. Said gas forces the graft (with forces of the order of mN) against the cornea, assuring a correct adherence and healing. The behaviour of the bubble of gas inside the AC is the manner which concerns this Thesis.

Since this text is directed to a non-medical audience, no explicit images of the procedure will be shown. Knowing every detail of the operation does not give any extra information to those with an engineering background nor is of great interest for the scope of this research. Therefore, if the reader is interested in acquiring more information about DMEK, please refer to Performing DMEK: A Step-by-Step Guide[4] by the American Academy of Ophthalmology. For sake of completness, Figure 1.1 shows a clip of Luis Buñuel's film *Un Chien Andalou* where the main actress is getting her eye cut.

[1]Department of Civil, Chemical and Environmental Engineering, University of Genoa, Italy.
[2]Department of Ophthalmology, Rigshospitalet, Glostrup, Denmark.
[3]Copenhagen Eye Foundation, Copenhagen, Denmark.
[4]A. Stuart, "Performing DMEK: A Step-by-Step Guide," *American Academy of Ophthalmology*, 08-Aug-2017. [Online]. Available: https://www.aao.org/eyenet/article/performing-dmek-stepbystep-guide. [Accessed: 28-May-2020].

Figure 1.1: Clip of the film *Un Chien Andalou* directed by Luis Buñuel Portolés and written by himself and Salvador Dalí i Domènech (Les Grands Films Classiques, 1929) showing Simone Mareuil getting her eye cut.

1.2 Anatomy of the anterior chamber

To correctly understand this text, the basic structure of the *vessel* containing the bubble must be described. The three main agents bounding the anterior chamber are: the cornea, the iris and the lens.

The cornea is the transparent layer in the front part of the eye. It lies anteriorly of the lens and pupil and plays a major roll in focusing the light for a correct vision. Its basic structure is made out of:

- **Epithelium:** Blocks the passage of foreign material and provides a smooth surface to absorb oxygen and nutrients from tears.
- **Brownman's Membrane:** Exclusive of primates, it is a smooth, acellular, nonregenerating layer without a clear purpose.
- **Stroma:** Due to its unique shape, arrangement, spacing and material it gives the cornea its light-conducting properties.
- **Descemet's Membrane:** It serves as a protective barrier against infections and injuries.
- **Endothelium:** Porous layer which pumps excess fluid out of the stroma. Without this pumping action, the stroma would swell with water and ultimately become opaque. It cannot be regenerated, therefore operations such as DMEK are available in the event it becomes injured.

During DMEK, the patient's endothelium and Descemet's membrane –the innermost layers of the cornea, see Figure 1.2– are removed giving place to the donor's

graft. After it is introduced, a bubble of air is injected into the AC. This is the chamber filled with aqueous humor, AH, bounded on top by the cornea and on the bottom by the iris and the pupil. The latter is the opening of the iris to the lens.

The lens is a transparent biconvex structure which refracts the light correctly into the retina. It is capable of changing the focal length of the eye by changing its shape thanks to a circular ring of muscle attached to it, known as the ciliary muscle. In some cases the lens can get damaged, which can lead to the classification of three types of eyes:

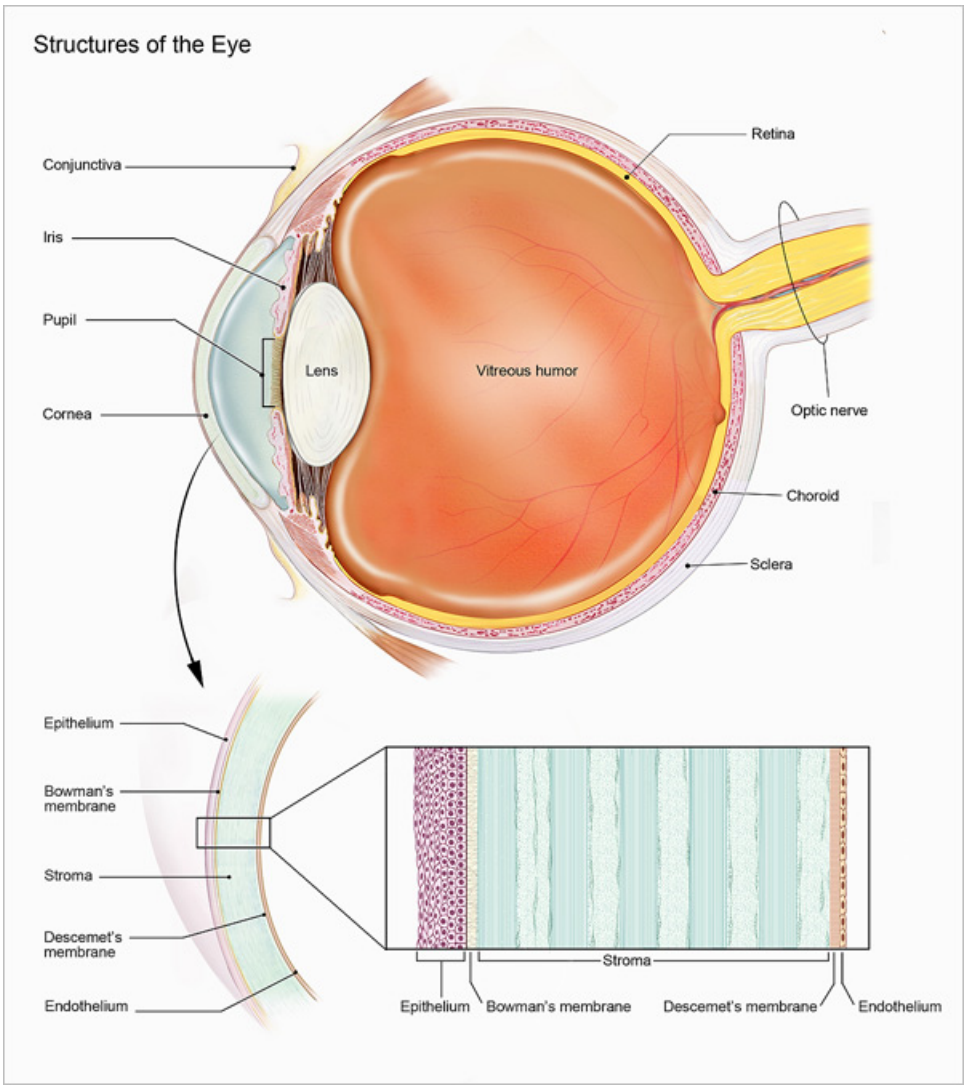

Figure 1.2: Basic anatomy of the eye and cornea.

- **Phakic:** From the Greek φᾰκός, *phakós*, "lentil, anything shaped like a lentil, in the sense on the lens". These patients present their own natural lens.

- **Pseudophakic:** From the Greek ψευδής, *pseudes*, "lying, false" and phakic. These patients have had an artificial lens implanted in the eye(s) to replace

their own natural one(s). The implanted lens is called an intraocular lens, IOL, or pseudophakic IOL.

- **Aphakic:** These patients do not present a lens and will not be part of this study.

This classification is crucial since it determines the geometry of the AC. The most relevant differences between patients with phakic and pseudophakic eyes are that the latter present a significant increase in the anterior chamber depth, ACD, and the trabecular-iris angle after surgery, Kurimoto et al. [3]. As it will be shown in later sections, this increase will be translated into the need of a more careful monitoring of the patient's position in order to optimize the graft coverage. In addition, one of the leading reasons for the removal of the lens is cataract surgery. The average age at which people get cataract surgery in the European Union is at 73.8 years old, Mojon-Azzi el at, [4]. Kanellopoulos et al. [5] found this variation in the ACD to be greater as age increased. The median age of the patients in the clinical trial this Thesis is based on, Alberti et al. [2], is 71 (minimum of 43 and maximum of 86), which reflects the age of DMEK patients in Denmark, home country of Dr. Alberti. Thus, elderly patients will be the ones with more need of position supervision but also the ones which show more apparent discomfort. Therefore, adding this constraint to the study will be crucial, specially for pseudophakic –elderly– patients.

The iris, is the annular structure behind the cornea and above the lens which defines the eye color. By contracting and expanding, it is responsible for controlling the diameter of the pupil. In an optic's sense, the pupil is the aperture and the iris the diaphragm.

Finally, the inherent nature of the AC makes it porous but also capable of pumping out liquid. Therefore, as the post-operative period advances the eye will naturally remove the gas from the anterior chamber. This time can go anywhere from 3 to 7 days depending on the gas injected and patient-specific features.

1.3 Scope of the research

DMEK is increasingly becoming the treatment of choice for corneal endothelial dysfunction. Compared with penetrating keratoplasty, endothelial keratoplasty provides optimal visual recovery, decreased healing time, smaller incisions and lower rates of rejection, Godinho et al. [6]. Since the first procedure was performed back in 2002 (Gerber-Hollbach et al. [7]), the ideal gas fill after DMEK and its dependence on the patient's AC geometry and position is still far from known, Pralits et al. [1]. In addition, the quantity of gas which is finally introduced is difficult –not to say impossible– to know a priori. Therefore, this Thesis will focus on determining a protocol to optimize the percentage of the graft covered by the gas at each point of

the post-op period as a function of the patient's AC geometry and position, having as a constraint the patient's *comfort*, which will be defined later on.

Moreover, as a final output, a set of easy-to-use materials, tables and graphs are hoped to be conceived for their clinical use. All the results and their presentation format have been heavily discussed with –and many proposed by– Dr. Alberti. Thanks to his insight and hands-on experience with the surgery, all results are hoped to be easy to interpret and manage by a non-engineering audience, especially by medical personnel, who are not necessarily familiar with the research.

Clinical aspects of this study involving patients adheres in accordance with the tenets of the Declaration of Helsinki.

2 | Materials and Methods

Disclaimer: Some fragments of this chapter have been taken directly from Pralits et al.[1], with the permission of its authors, as allowed by the licence protecting their study CC BY-NC-ND 4.0. As this Thesis is a direct continuation of the aforementioned publication in collaboration with said authors, most of the materials used are identical and, thus, are by no means acts of plagiarism.

In order to obtain the optimized position of the patient which maximizes the graft coverage for a given geometry and post-operative period, many different situations must be studied. Due to ethical constraints, this must not be performed on patients. In addition, patients would not yield controlled environments to have reliable results. Thus, the medical team outreached Prof. Pralits to use computational fluid dynamics, CFD, to simulate the behaviour of the bubble of air in the "vessel" which is the AC.

2.1 Geometries of the anterior chamber

Although the cornea is a flexible and porous tissue; the iris, contracts and expands in order to control the amount of light which passes trough the pupil; the ciliary muscle changes the shape of the lens to correctly focus the images, all surfaces are assumed to be infinitely rigid and idealized geometries of the anterior chamber have been used to model a phakic as well as a pseudophakic eye. The model representing a phakic eye is based on the geometry used in Repetto et al. [8] (Figure 2.1a), while the geometry of the pseudophakic eye (Figure 2.1b) has been taken from the investigation by Kapnisis et al. [9].

The geometries of the AC can be parameterized with the ACD, defined as the distance between the corneal epithelium and intraocular lens anterior surface, see Figure 2.1a. Taking this quantity as representative of the whole geometry, three models were simulated both for the phakic and pseudophakic cases. One of them –2.65 mm for phakic patients and 4.35 mm for pseudophakic ones– represents the average ACD in the Fuch's endothelial dystrophy patient population eligible for endothelial keratoplasty procedures involving air/gas in the AC, see Alberti et al. [2].

The other two values are the minimum and maximum ACDs in the aforementioned trial. The specific stereolithography files (STL-files) used in the simulations were ceded by Pralits et al. [1]. The geometric characteristics of both types of ACs are shown in Table 2.1.

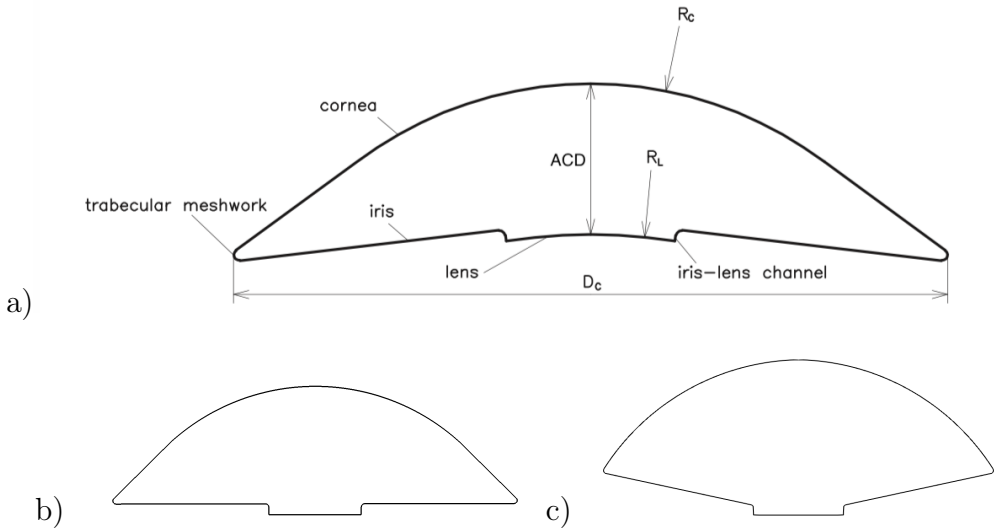

Figure 2.1: Symmetry plane of the anterior chamber geometries; (a) phakic eye including definition of dimensions (b) pseudophakic eye ACD = 3.45 and 4.35 mm (c) pseudophakic eye ACD = 5.00 mm. Both at the same scale, the pseudophakic one is considerably larger than the phakic and its lens is flat. See Table 2.1 for abbreviations and parameter values.

Table 2.1: Parameter abbreviations and values for the three phakic and pseudophakic AC geometries simulated.

Parameter	Abbreviation	Value
Geometrical characteristics of the phakic ACs		
Volume of the AC	V_{AC}	0.105/ 0.170/ 0.271 [mL]
Diameter of the AC	D_{AC}	12.5/ 12.5/ 12.5 [mm]
AC depth †	ACD	1.79/ 2.65/ 3.68 [mm]
Posterior cornea minimum radius of curvature ‡	R_C	6.8/ 6.8/ 6.8 [mm]
Radius of curvature of the natural lens	R_L	10.0/ 10.0/ 10.0 [mm]
Height of the iris–lens channel	-	0.10/ 0.10/ 0.10 [mm]
Angle between cornea and iris	-	16.2/ 28.6/ 47.9 [deg]
Geometrical characteristics of the pseudophakic ACs		
Volume of the AC	V_{AC}	0.219/ 0.279/ 0.309 [mL]
Diameter of the AC	D_{AC}	12.7/ 12.7/ 12.7 [mm]
AC depth †	ACD	3.45/ 4.35/ 5.00 [mm]
Posterior cornea minimum radius of curvature ‡	R_C	6.8/ 6.8/ 6.8 [mm]
Radius of curvature of the natural lens	R_L	$\infty/\ \infty/\ \infty$
Height of the iris–lens channel	-	0.24/ 0.24/ 0.24 [mm]
Angle between cornea and iris	-	45.8/ 55.1/ 69.5 [deg]

† Alberti et al.[2].
‡ Helmholtz [10].

2.2 Model description

The evolution of the fluids was computed numerically by solving the incompressible, isothermal Navier-Stokes equations for two immiscible fluids –i.e., mass conservation and momentum balance. While the fluid-gas interface was tracked using the Volume of Fluid (VOF) method. The governing equations are:

$$\nabla \cdot U = 0, \tag{2.1}$$

$$\rho \frac{\partial U}{\partial t} + \rho U \cdot \nabla U - \mu \nabla^2 U = -\nabla p_d - \rho g \cdot x + \sigma \kappa \nabla \gamma, \tag{2.2}$$

where U is the fluid velocity; ρ, the density; μ, the dynamic viscosity; p_d, the pressure; g, the gravitational acceleration; σ, the surface tension; κ, the curvature; and γ, the indicator function representing the volume fraction of one of the fluid phases, where

$$\gamma = \begin{cases} 1 & \text{if control volume is filled only with liquid} \\ 0 & \text{if control volume is filled only with gas} \\ 0 < \gamma < 1 & \text{if interface is present} \end{cases} \tag{2.3}$$

Table 2.2 shows the values of the fluid properties used.

The VOF method relies on solving the governing equations assuming a single effective fluid throughout the domain. Then, a generic fluid property χ (e.g., U, ρ or μ) is computed using a weight function, based on the volume occupied by each phase in a given numerical cell

$$\chi = \chi_l \cdot \gamma + \chi_g \cdot (1 - \gamma), \tag{2.4}$$

where the subscripts l and g represent the liquid and gas phase, respectively. The evolution of the indicator function γ is governed by an advection transport equation:

$$\frac{\partial \gamma}{\partial t} + \nabla \cdot (U\gamma) + \nabla \cdot [U_r (1 - \gamma)] = 0, \tag{2.5}$$

where the relative velocity term $U_r = U_l - U_g$ is active only in the interface region and increases the interface resolution; thus, avoiding special numeric treatment, Pralits et al. [1].

The numeric simulations were computed using the free open-source software OpenFOAM's[1] `interfoam` solver. The discretization of the domain is performed

[1] OpenCFD Ltd, available in the public domain at http://openfoam.com

with the mesh generation utility `snappyHexMesh`. As shown in Figure 2.2, the workflow followed by this algorithm is:

1. Generation of a base (background) mesh.
2. Definition of the geometry of the AC in STL-file form.
3. Generation of a castellated –cartesian– mesh.
4. Generation of a snapped –body-fitted– mesh.
5. Addition of layers near the surface.
6. Enforce mesh quality.

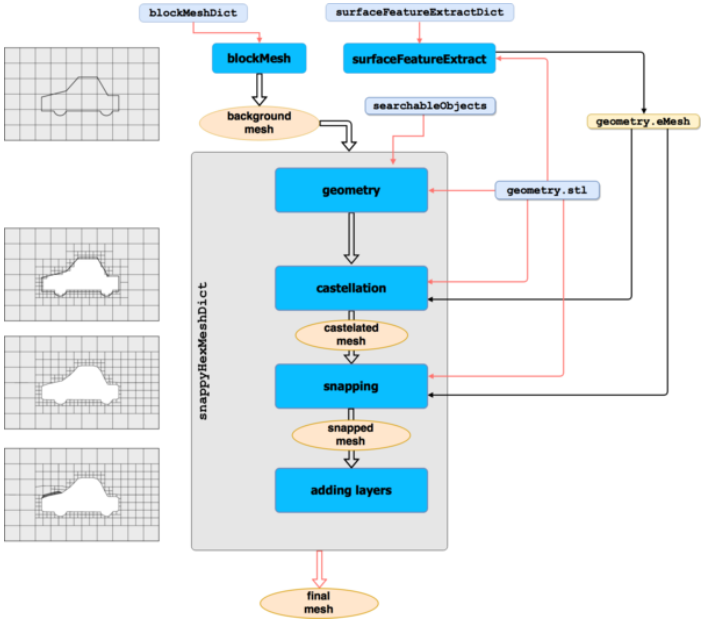

Figure 2.2: Workflow of the `snappyHexMesh` algorithm and example, retrieved from [11].

Before running the code in parallel at Politecnico di Milano's DAER (Milan, Italy) and Università di Genova's DICCA (Genoa, Italy), a careful sensitivity analysis was conducted to numerical and physical parameters. The viscosity, mesh and number of cores used were obtained by optimizing the CPU time required to reach equilibrium while minimizing the error. Large viscosities yield slow evolution towards the final position while small ones force a rapid transitory period and associated physical oscillations. Thus, a compromise had to be done. Figure 2.3 shows the speedup curve of the CPU time required vs. the number of cores used, for a comparable but much shorter simulation: *Syphon effect (flushing a tank) using interFoam*[2].

[2]Pralits, J. & Guerrero, J. (2020) *Multiphase flows modeling in OpenFOAM: Guided Tutorials* [Course Material] Wolf Dynamics, Università degli studi di Genova, Genoa (GE), Italy.

Then, the sensitivity of the solution to the contact angles was performed. To date there are no clinical trials which have determined the contact angle at the iris. Therefore, using the ansatz that the contact angle is equal to the one at the lens, Miyake et al. [12],

$$\alpha_{\text{iris}} = \alpha_{\text{lens}} = 24°,$$

the dependence of the solution to real value was performed. It was found that the variations in the equilibrium position were negligible, at least in $\alpha_{\text{iris}} \in [15°, 35°]$. The final value was chosen attending to computational cost restrictions.

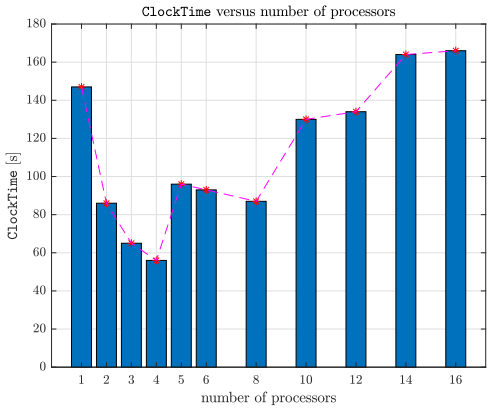

Figure 2.3: Speedup curve of the CPU time required vs. the number of cores used.

Unlike with the iris, clinical trials have been conducted to experimentally obtain the contact angle at the cornea, α_{cornea}. Observations performed by Alberti et al. [2], as shown Figure 2.4, found a contact angle based on patient measurements with anterior segment optical coherence tomography, OCT, to be:

$$\alpha_{\text{cornea}} = 16.81° \pm 3.11°. \tag{2.6}$$

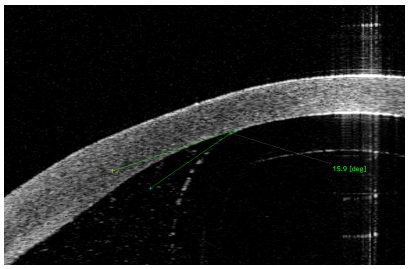

Figure 2.4: Measurement of the contact angle at the cornea measured using OCT, Alberti et al. [2]. The exterior thick layer is the cornea while the thin diffuse interior white line is the gas-liquid interface.

While increasing the contact angle at the cornea drastically decreases the simulation time, a considerable variation was found in the equilibrium state. Therefore, respecting the clinical trials and according the the results found in the aforementioned sensitivity analysis, $\alpha_{\text{cornea}} = 17°$ will be used.

In view of the past results, a suggestion could made: refining the measurement of the contact angle at the cornea seems much more critical than exhausting resources in order to obtain novel quantities for the iris. Since the final equilibrium position does not appear to be as dependant to the contact with a flat surface –iris– as it is to a curved one –cornea.

Table 2.2: Fluid properties and their values (referenced when necessary) used in the simulations.

Parameter	Abbreviation	Value
Aqueous humor properties		
Density†	ρ	1000 [kg/m^3]
Kinematic viscosity‡	ν	$1.4 \cdot 10^{-4}$ [m^2/s]
Air properties		
Density†	ρ	1.225 [kg/m^3]
Kinematic viscosity‡	ν	$1.4 \cdot 10^{-4}$ [m^2/s]
Surface tension with AH†	σ_{air}	0.07 [N/m]
Iris contact angle	α_{iris}	20°
Lens contact angle (phakic)§	α_{lens}	24°
Lens contact angle (pseudo)	α_{lens}	24°
Cornea contact angle¶	α_{cornea}	$16.59° \pm 3.20°$

† Spandau [13].
‡ A *numerical* viscosity was used instead to optimize the computational cost. A proper sensitivity analysis was performed to asses the validity of this modification.
§ Miyake et al. [12].
¶ Alberti et al.[2].

The numerical simulations were launched by fixing a volume ratio (ratio of the volume of gas to the total volume of the domain), initially setting a horizontal shape at the interface and varying the gravitational vector instead of the AC's position. Sensitivity analyses to the shape and position of this initial injection point were also performed. The study concluded the equilibrium position was robust to changes in the initial position. This is in some way a transcendental finding, since if it was not true this Thesis would not be valid. Not only if the gas departs from this initial flat position it will arrive to the same equilibrium position, but from any other equilibrium position it would always arrive univocally to the same state – for the same set of prescribed conditions, of course.

Advancing in time, the interface evolves towards its equilibrium shape; when a

steady solution is obtained, the simulation ends. The equilibrium condition is set such that the percentage of each surface –cornea, iris and lens– being covered by the gas is invariant with time, see Figure 2.5. This procedure takes about 3 seconds and it is when the value of the viscosity is most critical: large viscosities would delay the convergence while small ones would introduce an oscillatory pattern. Both would increase the relaxation time and, thus, the computational cost.

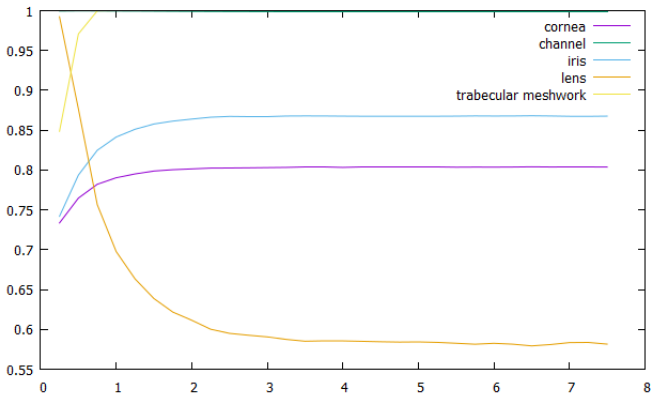

Figure 2.5: Convergence of the simulation as invariance of the coverage of its surfaces, condition for the termination of the simulation.

2.3 Parameters and Observables

As stated in Chapter 1, the objective is to optimize the coverage of the graft[3] as a function of the AC geometry, the patient's position and the post-operative period. The geometry of the AC has already been characterized by the ACD. The post operative period, will be represented by the gas filling ratio: volume of gas to total volume,

$$\varphi := \frac{V_{\text{gas}}}{V_{\text{AC}}}, \quad \varphi \in [0,\, 1]\,.$$

This parameter can be thought of as a non-dimensional time: right after the surgery, the gas filling ratio is maximum and very difficult to determine clinically; as the post-op period advances, its value decreases until no bubble is present at the AC and $\varphi = 0$. Finally, the position of the patient will initially be given exclusively by the gaze angle, ψ. However, it will be extended to other degrees of freedom. As Figure 2.6 shows, the gaze angle is defined with respect to gravity. Thus, $-90°$ represents the supine position; $0°$, the horizontal gaze; and $90°$, the prone position.

[3]Assumed to always have a 8.5 mm diameter (independently of the patient) and centered at the cornea.

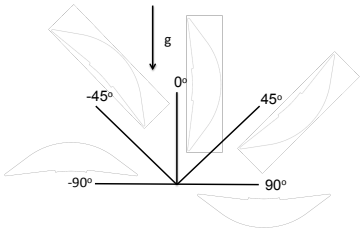

(a) Position of the anterior chamber with respect to gravity, Pralits et al. [1].

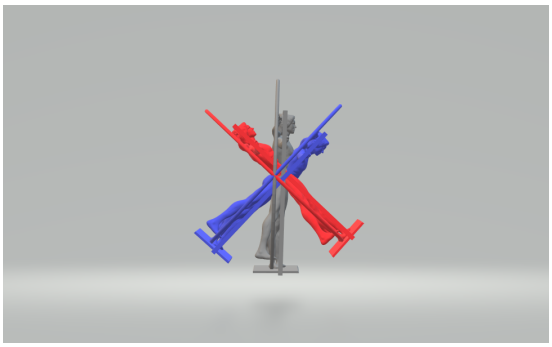

(b) Position of the patient: red negative gaze angle and blue positive, CAD model from [14].

Figure 2.6: Definition of the gaze angle, ψ. Thus, $-90°$ represents the face-up position; $0°$, the horizontal gaze; and $90°$, the face-down position.

The current research is focused on evaluating the graft coverage for all the geometries present in the eligible patients of Alberti et al. [2] and all the positions, i.e.,

$$\begin{aligned} \max_{\psi} \quad & \text{graft coverage} \\ \text{s.t.} \quad & \text{given ACD}, \varphi \ \wedge \ \text{comfort} \end{aligned} \tag{2.7}$$

For each of the mentioned ACDs, a set of 5 gas filling ratios will be studied following Chebyshev's nodes distribution in $\varphi \in [0.15,\ 0.85]$,

$$\varphi_k = \frac{1}{2} + \frac{7}{20}\cos\left(\frac{2k-1}{10}\pi\right), \quad k = 1, ..., 5. \tag{2.8}$$

Chebyshev nodes are popular in aeronautical applications, especially in the study of airfoils, since they concentrate the majority of their nodes at the the leading and trailing edges. In this case, the gas filling ratios are focused towards the beginning and end of the post-op period where the bubble's dynamic has been seen to change more sharply. For each φ, 15 linearly spaced gaze angles will be studied. Since the equilibrium state does not depend of the initial position, each gas filling ratio-gaze angle-ACD trio can be studied independently. This is, first by letting them arrive to equilibrium separately and then comparing them as continuous phenomenon.

The comfort term in Equation 2.7 is not a universal condition but rather a patient-specific one. The reader must imagine the following situation: the solution to the optimization problem yields that in a given post-op period, φ, the patient must be positioned at exactly $\psi = 43°$. However, in that same period lying down facing up only implies a 5% decrease in the graft coverage. Is it reasonable, then, to force the patient to be in an uncomfortable position? To this discussion it must be

added, as stated in Chapter 1, that most of the patients are elderly and these post-op periods can go for as long as a week. Therefore, suboptimal solutions will also be given which to this humble *tesisti*, and with the observations of Dr. Alberti, seem much more feasible. This concept is known as therapeutic adherence: "the extent to which the patient follows medical instructions", as defined by the World Health Organization [15]. This compliance was found to decrease with physical discomfort, Christensen [16]. Therefore, alternatives must be given.

Currently, it is not possible to clinically measure the volume of gas present in the AC after DMEK. Therefore, two parameters are proposed by Pralits et al. [1] to indirectly represent φ, namely: H_m, which is the vertical height from the inferior of the bubble to the superior chamber angle, and H_c, which is the vertical height from the inferior gas-cornea contact angle to the superior chamber angle, see Figure 2.7. The value of H_c can be obtained clinically using a slit-lamp while H_m is obtained from AS-OCT, both are measured with the patient looking straight ahead (i.e., $\psi = 0°$). Pralits et al. [1] discuss the advantages and disadvantages of both techniques.

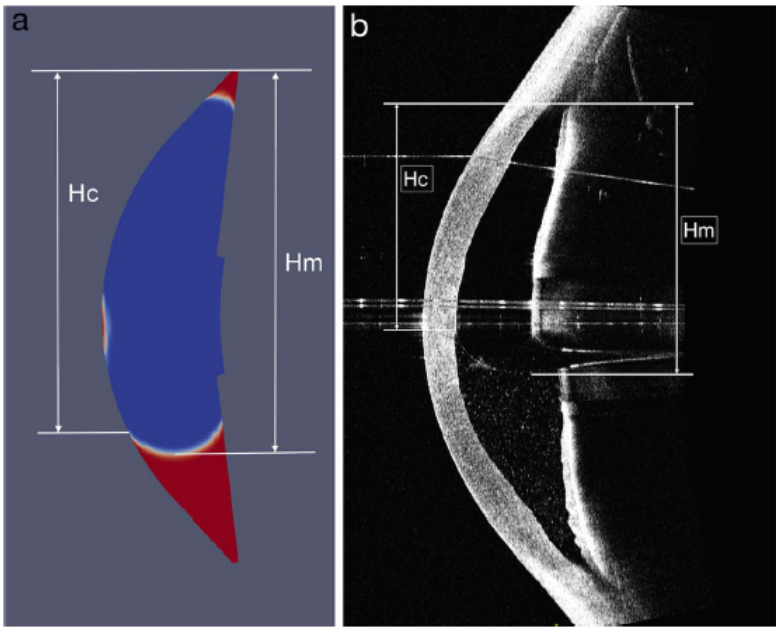

Figure 2.7: Definitions of H_c and H_m. To the left the numerical measurement, to the right the same image but obtained from Optical Coherence Tomography (OCT). Retrieved from Figure 3 in Pralits et al. [1].

Figure 2.8 and Figure 2.9 show the values of H_c and H_m –non-dimensionalized with the diameter of the AC– as a function of the ACD and the gas filling ratio, for phakic and pseudophakic patients respectively. Clinical validations of these results are shown in Pralits et al. [1]. These results are a generalization of their findings.

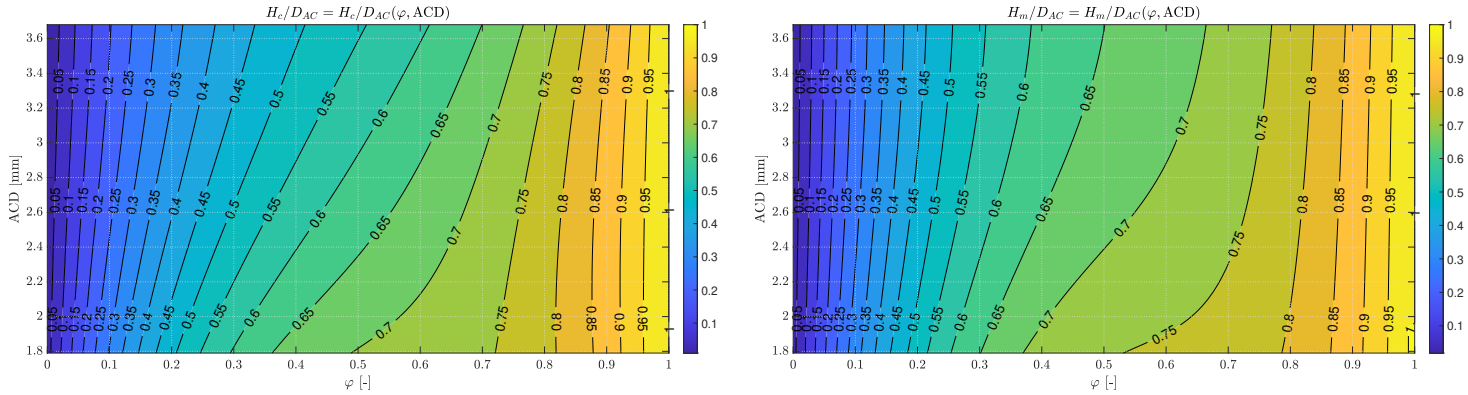

(a) Isoheight curves representing $\frac{H_c}{D_{AC}} = \frac{H_c}{D_{AC}}(\mathrm{ACD}, \varphi)$ (b) Isoheight curves representing $\frac{H_m}{D_{AC}} = \frac{H_m}{D_{AC}}(\mathrm{ACD}, \varphi)$

Figure 2.8: Distribution of the values of $\frac{H_c}{D_{AC}}$ and $\frac{H_m}{D_{AC}}$ as a function of the gas filling ratio and the ACD for phakic patients

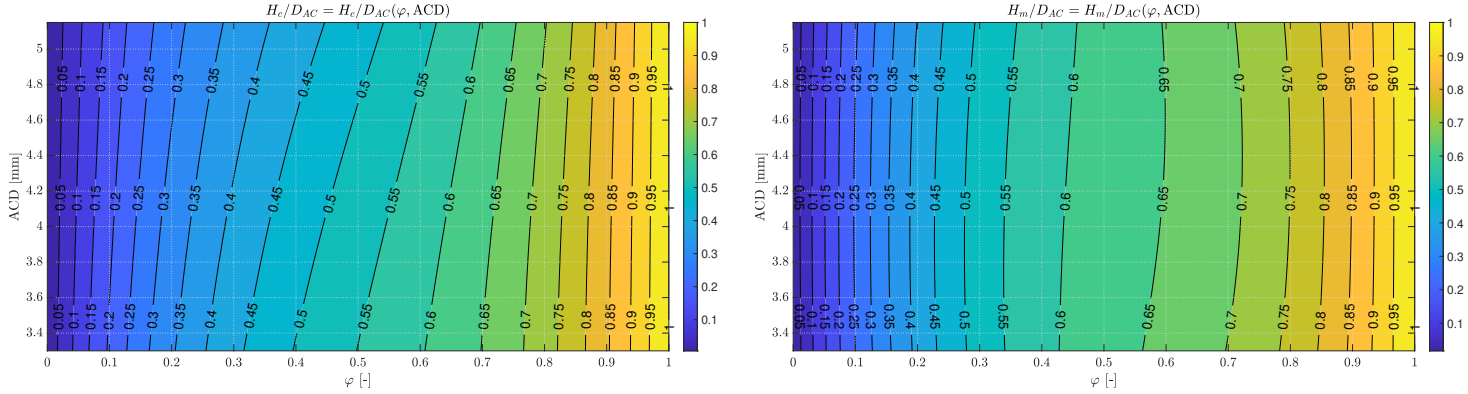

(a) Isoheight curves representing $\frac{H_c}{D_{AC}} = \frac{H_c}{D_{AC}}(\mathrm{ACD}, \varphi)$ (b) Isoheight curves representing $\frac{H_m}{D_{AC}} = \frac{H_m}{D_{AC}}(\mathrm{ACD}, \varphi)$

Figure 2.9: Distribution of the values of $\frac{H_c}{D_{AC}}$ and $\frac{H_m}{D_{AC}}$ as a function of the gas filling ratio and the ACD for pseudophakic patients

2.4 Characterization of the position of the bubble

Currently, Pralits et al. [1] have been able to evaluate the percentage of the graft being covered by the gas. Phenomena like graft detachment or air penetration in between the graft and the cornea demonstrate it may not be enough to know exclusively how much of the bubble is covering by graft but also where.

In order to position the 3D intraocular bubble inside the AC, its projection on the cornea will be used. In general, this projection will be an ellipse. An algorithm can be constructed to detected said ellipse exploiting the `Image Processing Toolbox` in MATLAB[4]. The method starts by obtaining a consistent screenshot of the equilibrium state of the projection, using the `Trace` capabilities of the open-source results visualization software Paraview[5]. Then a consistent 484 x 551 pixel image is cropped from the original.

This code aims to detect the white boundary which separates the gas from the AH (in Paraview red is 100% of AH; blue, 100% gas; and white, the transition between both). Therefore, for a more effective detection, the image is converted to a gray scale using the `rgb2gray` function in MATLAB, see Figure 2.10c. In this format, the pixel information is simpler than a complete RGB image and the contrast between the boundaries is clearer.

In gray scale images, each pixel's value is a single number that represents its brightness. The most common pixel format –and that used by MATLAB– is the byte image, where this number is stored as an 8-bit integer giving a range of possible values from 0 to 255. Zero is taken to be black, and 255 is taken to be white. Values in between make up the different shades of gray.

Once the image is in gray scale, the pixels are discriminated in basis of if they are more white or more black than a certain threshold pixel brightness. The northernmost pixel will be the top of the projection of the bubble; while the easternmost one, the left part; and so on. With the information of these four pixels the rest of the ellipse can be totally defined by the semi-major axis a, the eccentricity e, and the position of its center $\mathbf{x_c}$ with respect to the center of the AC. If the allowed movement of the patient is restricted to pitch, as described in Figure 2.6, the bubble will only move in the vertical axis. Thus, $\mathbf{x_c} = (0,\ y_c)\Big|_{\psi}$.

The code also allows for the manual insertion of the points if the user is not satisfied with the pixels found. An example of the implementation of this method is shown in Figure 2.10.

[4]Version R2019b; Mathworks Inc., Natick, MA, USA.

[5]Version v5.8.0-RC2; Sandia National Labs, Kitware Inc, and Los Alamos National Labs., available online at http://paraview.org.

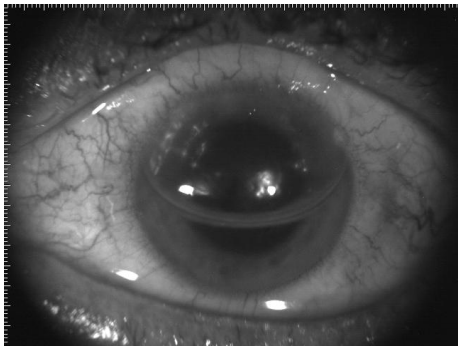

(a) Near infra-red image of a patient's eye after DMEK, ceded by Alberti et al. [2].

(b) Numerical recreation of the patient's AC and its equilibrium state.

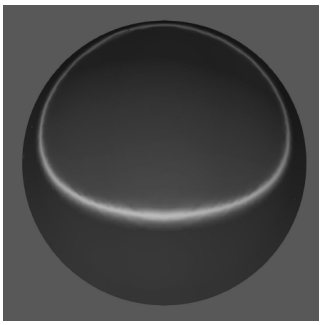

(c) Gray-scale screenshot for ellipse detection.

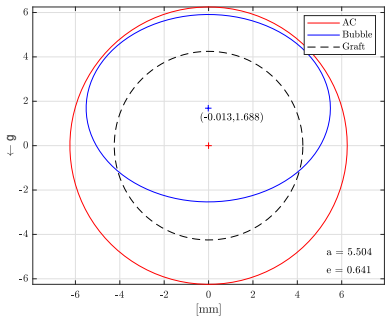

(d) Characteristic dimensions of the projection of the bubble on the cornea.

Figure 2.10: Example of the employment of the ellipse detection method on a phakic patient with an ACD = 3.68 mm and a gas filling ratio of $\varphi = 0.68$.

3 | Results

This chapter describes the shape, size and position of the projection of the bubble on the cornea as well as the percentage of the graft being covered as a function of the patient's ACD, position and post-op period for both AC cases.

3.1 Interpolation of the numerical results

After running a finite number of simulations (179 for phakic patients and 183 for the pseudophakic ones) a finite set of equilibria are obtained. As stated in Chapter 2, the independently run situations will be taken as continuous considering the initial conditions do not affect the equilibrium states. A *concatenated polynomial fitting* is proposed to interpolate the results. Let χ be a generic value (e.g., the position of the bubble, its size, the graft coverage...) for a given phakic or pseudophakic patient. This generic variable can be set to be $\chi = \chi\,(\mathrm{ACD},\, \psi,\, \varphi)$ following the next fits

$$\chi\,(p_k,\, \varphi) = [p_1 \;\; p_2 \;\; p_3 \;\; p_4] \begin{bmatrix} \varphi^3 \\ \varphi^2 \\ \varphi^1 \\ \varphi^0 \end{bmatrix}, \tag{3.1}$$

where

$$p_k\,(a_k,\, b_k,\, c_k,\, d_k,\, \psi) = a_k\,\psi^3 + b_k\,\psi^2 + c_k\,\psi + d_k, \quad k = 1, 2, 3, 4. \tag{3.2}$$

Then, the coefficients a_k, b_k, c_k and d_k are fitted to the ACD. Due to time limitations, only three geometries have been studied so they will be fitted to a parabola. However, this may lead to what is known in statistics as *overfitting*: "the production of an analysis that corresponds too closely or exactly to a particular set of data, and may therefore fail to fit additional data or predict future observations reliably", as defined by the Oxford Dictionary. Therefore, this final step must be taken with care. Nevertheless, it has been checked to be consistent with the observations inside the

extreme ACDs studied, i.e., the maxima and minima found in the eligible patients by Alberti et al [2]. Thus, the coefficients in Equation 3.2 are finally fitted to

$$\underline{v}\,(\underline{\sigma},\ \mathrm{ACD}) = \underline{\sigma} \begin{bmatrix} \mathrm{ACD}^2 \\ \mathrm{ACD}^1 \\ \mathrm{ACD}^0 \end{bmatrix}, \quad k = 1, 2, 3, 4. \tag{3.3}$$

where $\underline{v} = [a_k,\ b_k,\ c_k,\ d_k]$ and $\underline{\sigma} = [\alpha_k,\ \beta_k,\ \gamma_k]$.

The procedure is schematized in the flowchart in Figure 3.1. The rounded out red rectangle represents the initial choice between phakic or pseudophakic eye as well as the desired value, which determines the coefficients. The green diamonds are the *decision* inputs introduced by the user. The orange rectangles are the *process* equations into which introduce the inputs and the parameters obtained in the previous step. The blue trapezoids are the output *data* of the equations.

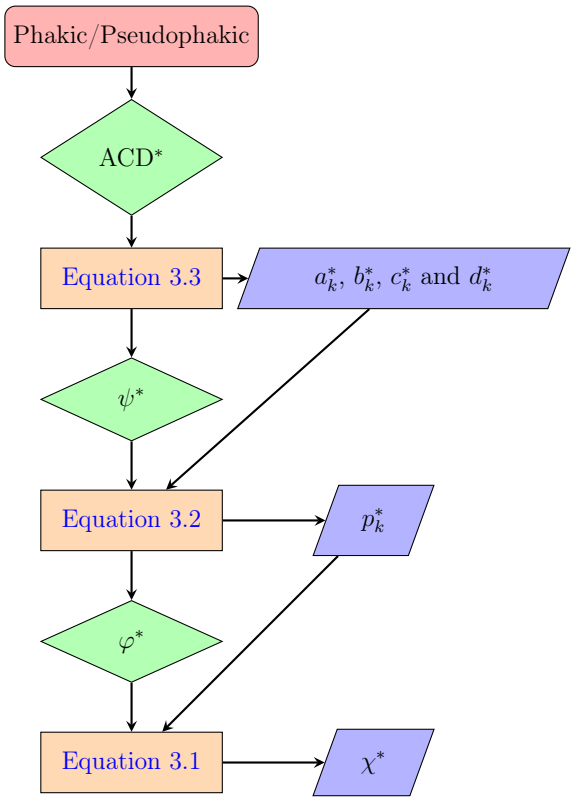

Figure 3.1: Flowchart of the different steps to obtain the desired solution χ^*.

In conclusion, the size, shape and position of the projection of the bubble on the cornea as well as the graft coverage are now completely described by a series of matrices $\mathbf{A} \in \mathbb{R}^{16\mathrm{x}3}$, defined by the α, β, γ trio for each coefficient a_k, b_k, c_k, d_k and for $k = 1, 2, 3, 4$, thus 16x3. The exact values for the coefficients used for the ACD in millimeters, the gaze angle in radians and the gas filling ratio in mL/mL are

shown in Appendix B. To date no clinical comparison has been conducted to asses the quality and validity of these results. However, Appendix D shows a numerical cross-validation which has yielded similar findings.

3.2 Phakic patients

The contours of gas-graft coverage –i.e., S_{air}/S_{graft}– (in percent) are shown in Figure 3.2 as a function of the gaze angle, ψ, and the gas filling ratio, φ. For small ACDs the graft coverage has a certain symmetry around $\psi = 0°$ and the coverage is almost insensitive to the position of the patient, being dominant the gas filling ratio (as it determines the size of the bubble, see Figure 3.3b). As the ACD increases, this symmetry is broken and the position of the patient gains importance. For example, a phakic patient with an ACD = 4 mm –Figure 3.2d– can experience differences of up to 35% depending on how s/he is oriented. In most cases, it is beneficial (in a graft coverage perspective) to be lying down face-up, $\psi = -90°$. For $\varphi > 0.8$ the graft can be totally covered by the bubble for some or all gaze angles, independently of the ACD. The dented contour lines representing 100% are artificial, since where the interpolation predicted coverages slightly greater than 100 ($\approx 105\%$) they were maxed out.

The reduction on the graft coverage when facing down, $\psi = 90°$, as the ACD increases can be attributed to the increase of the eccentricity. As the patient's pitch increases, the bubble transitions from being settled on the cornea to be placed on the iris and lens, see Figure 3.3c and d. Large ACDs imply larger available volume, V_{AC}, and, therefore, the curvature of the 3D intraocular bubble has more space to enclose itself which results in smaller projections of the bubble on the cornea with more eccentricity. The percentage of the graft being covered by air is defined as[1]

$$S_{\text{air}}/S_{\text{graft}} = \frac{\pi ab}{\pi R_g^2} = \left(\frac{a}{R_g}\right)^2 \sqrt{1-e^2}.$$

For a fixed gas filling ratio, the variation in the semi-major axis is in the order of 10^{-4} m, see Figure 3.3b. Therefore, $\frac{a}{R_g}\Big|_{\text{fixed }\psi} \approx$ const. which allows the relationship

$$S_{\text{air}}/S_{\text{graft}} \propto \sqrt{1-e^2}.$$

Thus, as V_{AC} increases, being pressured more or less against the cornea implies great differences in the eccentricity. As the eccentricity rises, less effective area is available for the correct coverage of the graft. Note the areas of low and high eccentricity in Figure 3.3a and its implications on the graft coverage in Figure 3.2d.

[1] More precisely, as the minimum between that and 100%, to account for projections larger than the graft.

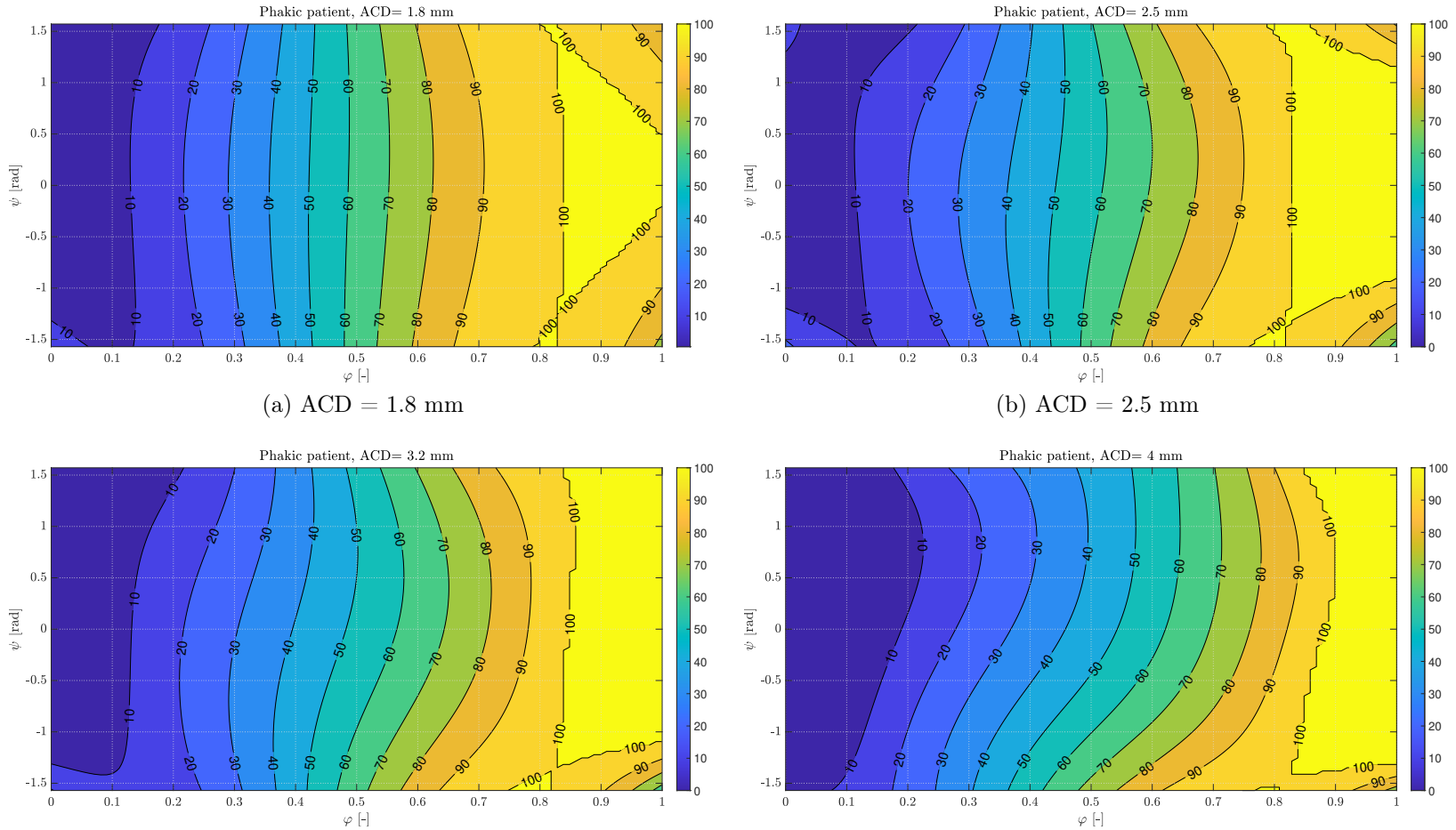

(a) ACD = 1.8 mm

(b) ACD = 2.5 mm

(c) ACD = 3.2 mm

(d) ACD = 4.0 mm

Figure 3.2: Isocoverage curves [%] in the $\varphi - \psi$ space representing $graft = graft(\varphi, \psi)$ (i.e., coverage of the graft by the bubble) for phakic patients for 4 different ACDs.

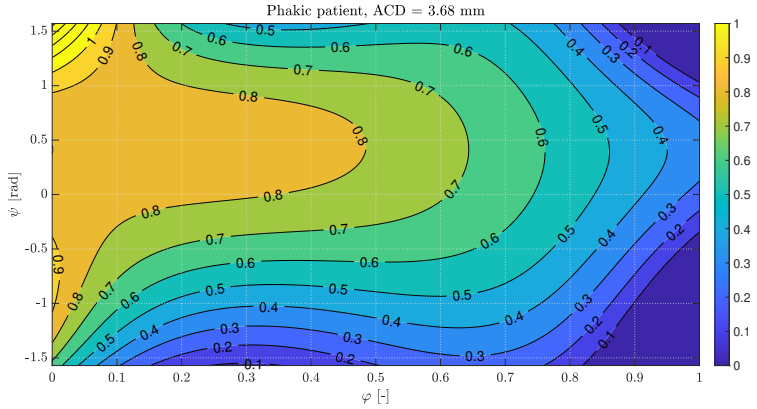

(a) Isoeccentricity curves

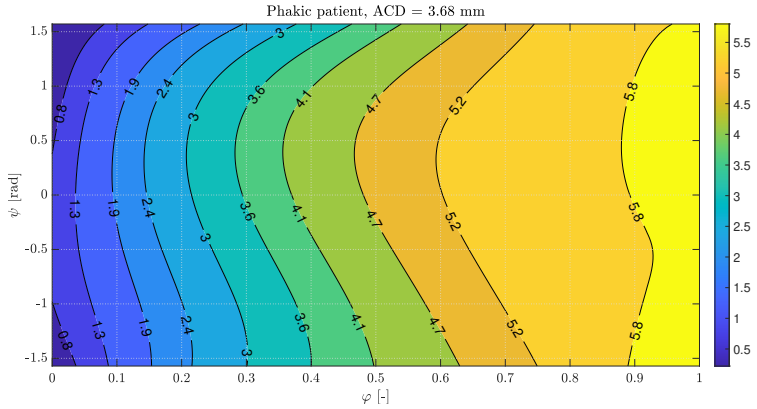

(b) Isosemi-major axis curves.

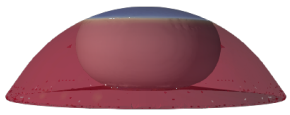

(c) $\psi = -90°$, $\varphi = 0.37$

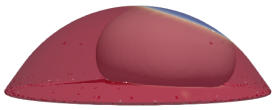

(d) $\psi = 90°$, $\varphi = 0.37$

Figure 3.3: Configuration of the bubble in the AC and the shape and size [mm] of the projection on the cornea in the $\varphi - \psi$ space for a phakic ACD = 3.68 mm eye.

3.3 Pseudophakic patients

The same discussion made for the phakic patients can be adapted to the pseudophakic ones. Patients lacking a natural lens tend to have larger ACDs and V_{AC} –even when comparing the same ACD, due to the flatting of the iris, see Figure 2.1b. This implies the position of the patient can dominate over the gas filling ratio. As Figure 3.4d shows, a pseudophakic eye with an ACD = 5.2 mm and a $\varphi = 0.4$, can range from having half of the graft covered to no coverage at all. Unlike the phakic case, even small pseudophakic ACDs suffer up to 25% variation of the coverage if the position of the patient is not taken care of. This is critical for large ACDs.

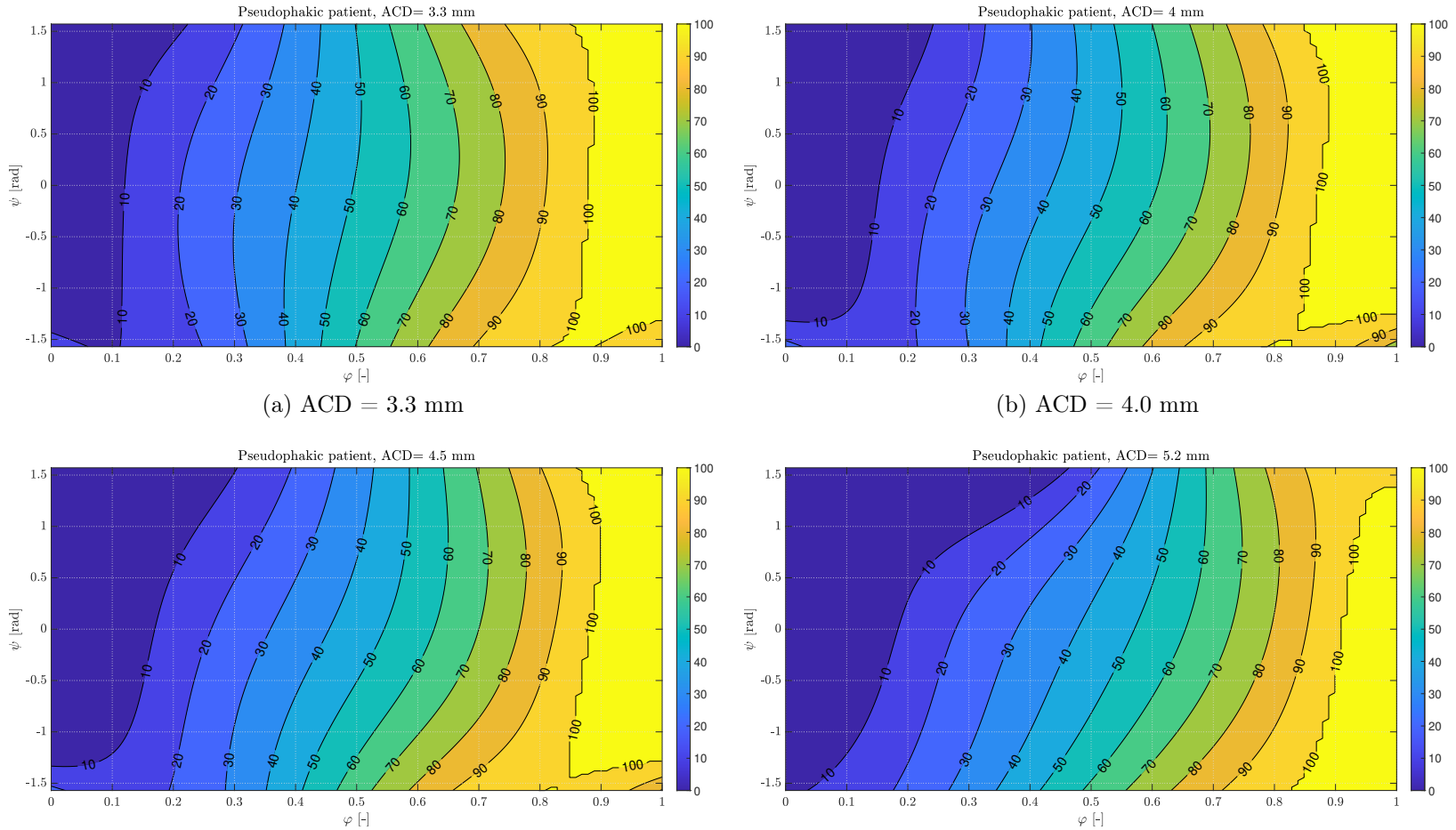

(a) ACD = 3.3 mm

(b) ACD = 4.0 mm

(c) ACD = 4.5 mm

(d) ACD = 5.2 mm

Figure 3.4: Isocoverage curves [%] in the $\varphi - \psi$ space representing $graft = graft(\varphi, \psi)$ (i.e., coverage of the graft by the bubble) for pseudophakic patients for 4 different ACDs.

3.3.1 Bubble detachment of the cornea

Figure 3.4 shows the advance of a 0% graft coverage pool as the ACD increases and the gas filling ratio decreases. The rise in the available AC volume allows the bubble to be totally set on the lens/iris. This phenomenon for the phakic case –and larger gas-filling ratios in the pseudophakic case– only meant larger eccentricities. However, the acceleration of the areas where the DMEK healing procedure fails increases rapidly in pseudophakic patients. Figure 3.5 shows the process in which the movement of the patient towards the prone position triggers the bubble to not touch the cornea, which has been called here *bubble detachment*. Figure 3.6 shows slices of the same process.

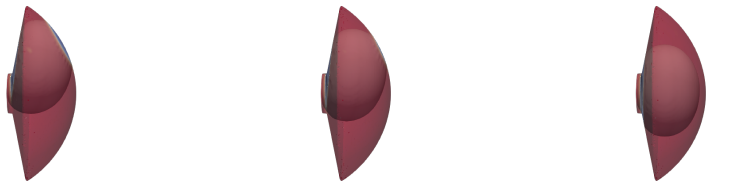

(a) $\psi = +72°$. (b) $\psi = +82°$. (c) $\psi = +90°$.

Figure 3.5: Bubble detachment process in a pseudophakic eye with an ACD = 5 mm and $\varphi = 0.37$.

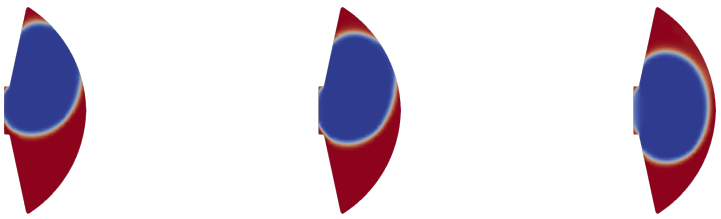

(a) $\psi = +72°$. (b) $\psi = +82°$. (c) $\psi = +90°$.

Figure 3.6: Slices of the process shown in Figure 3.5.

This phenomenon posses an inconvenience in the model used in this Thesis. The existence of the projection of the bubble on the cornea is an underlying assumption. When the bubble does not touch the cornea there is nothing to which attribute the position of the center or the shape and size. Before seizing to exist, as shown in Figure 3.6, the projection abruptly becomes smaller and smaller. Therefore, it is safe to assume that when the semi-major axis tends to zero the projection of the bubble stops existing:

$$a \lessapprox 0 \rightarrow \nexists \text{ projection.} \tag{3.4}$$

This condition is not enough by itself, since the polynomial fit artificially creates very large bubbles around the discontinuity formed by setting $a = 0$ –the condition for the removal of the projection. However, these bubbles are predicted to have an eccentricity larger than one, a hyperbola. Phenomenon consistent with the projection not being captured correctly by the elliptic model. It is safe to assume, then, the bubble will also not be in contact with the cornea. Thus, the following condition is added

$$e \gtrapprox 1 \rightarrow \nexists \text{ projection.} \tag{3.5}$$

If one or both of the two conditions are met, the system is overwritten: the graft coverage is set to zero and the semi-major axis, the eccentricity and the position of the center are set to `NaN`.

Figure 3.7 shows an example of how the model fails near the regions where the projection was observed to stop existing. The model predicts a graft coverage of 17% but, as it is observed in the figure, the bubble is not in contact with the cornea. The predicted semi-major axis is 0.28 mm. Thus, supporting this condition alone is not enough to determine if the bubble is touching the cornea or not. The foreseen eccentricity is 1.01. Therefore, the described conditions are able to asses the validity of the results and they would overwrite the model in this case.

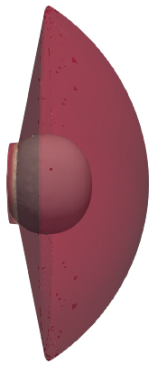

Figure 3.7: Example of bubble detachment in a pseudophakic eye with ACD = 5 mm, $\varphi = 0.08$ and $\psi = 90°$.

The area in the $\varphi - \psi$ space where the conditions predict the bubble is not in contact with the cornea increases as the ACD is enlarged. Reaching the extreme situation where the ACD is so large the bubble never touches the cornea, phenomenon present in patients with an ACD larger than 8 mm. However, for ACD $\approx$ 6 mm this circumstance occurs below $\varphi = 0.5$ for all gaze angles, according to this Thesis' model using the coefficients in Appendix B. Luckily, Savini et al. [17] found the probability to have an ACD even greater than 5.4 mm to be less than 1%. However,

the same study found 12.8% of pseudophakic patients to have ACDs larger than 5 mm, which have large regions of no contact for $\varphi < 0.5$ and $\psi > 60°$, see Figure 3.4d.

3.4 Maximum graft coverage trajectory

This procedure has been inspired by the trajectory regulation implemented in wind turbines to obtain the maximum power in a Cp-TSR plot, see Hemani [18] for example. Therefore, this section will emulate a control system by yielding the optimal gaze angle, ψ, for every instant of time –represented by the gas filling ratio, φ– which maximizes the graft coverage for a given AC geometry.

Figure 3.8 presents an example of the maximum graft coverage trajectory. Every dot on the isocoverage contours represents the gaze angle which maximizes the graft coverage for a given gas filling ratio. The plot shows a large area covered for $\varphi > 0.8$. This topology reminds of the mathematical chaos present in the equilibrium points of the logistic map. However, the reason behind these bifurcations has a radically different explanation. Simply, at some gas filling ratios many gaze angles provide a complete coverage of the graft. Despite this discussion, patients rarely present these large values of φ since the initial injection is normally below $\varphi = 0.8$.

Figure 3.9 shows the evaluation of the maximum graft coverage trajectory as a function of the ACD for phakic and pseudophakic patients. The trend is such that as the ACD increases, the optimal position tends to be lying down facing up. As observed in Figure 3.9b, pseudophakic patients –as they present larger ACD and V_{AC}– with an ACD $\gtrapprox 4.5$ should optimally have a $\psi = -90°$ in order to have maximum graft coverage. These trajectories could be achieved, for example, by inclining the hospital bed.

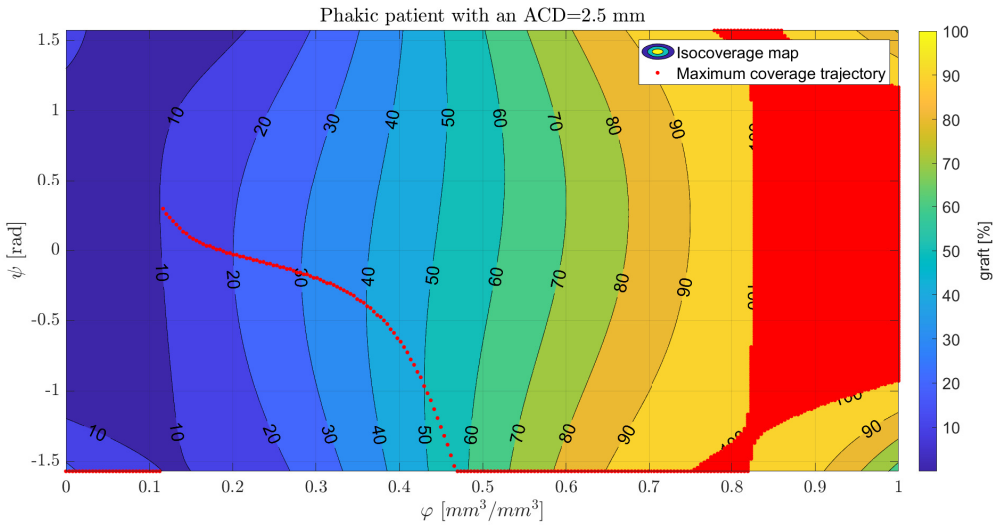

Figure 3.8: Maximum graft coverage trajectory for a phakic eye with an ACD = 2.5 mm. Plotted on the isocoverage contour graph.

The maximum graft coverage trajectory shows the optimal scenario. However, the same can be obtained for the minimum graft coverage trajectory which, on the other hand, would exhibit the worst-case scenario. Figure 3.10 displays the time-average graft coverage (i.e., the mean coverage over all gas filling ratios) when using the maximum and minimum graft coverage trajectories. The theoretical maximum mean graft coverage achievable is basically the same independently of the ACD and having a natural or artificial lens, presenting a 5% maximum difference. Therefore if the optimal gaze angle is used, the graft will be covered on average 60%. However, the minimum mean graft coverage decreases drastically as the ACD increases.

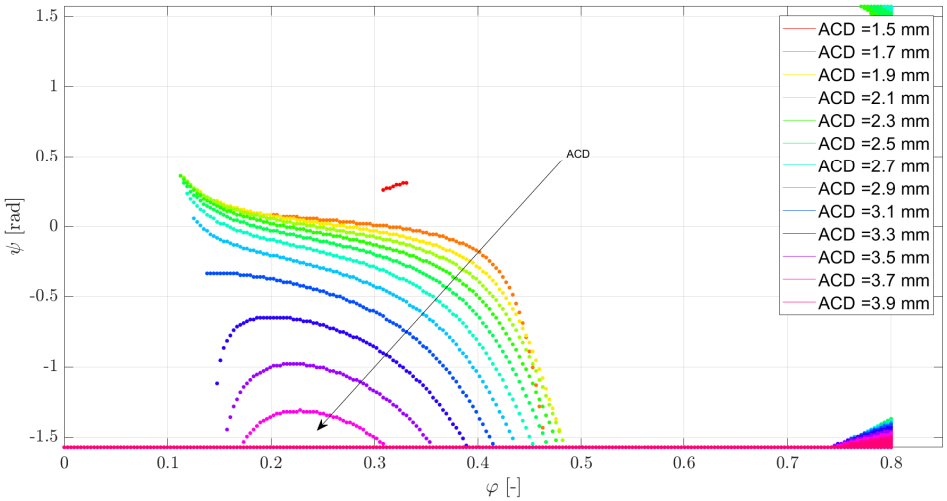

(a) Phakic patients

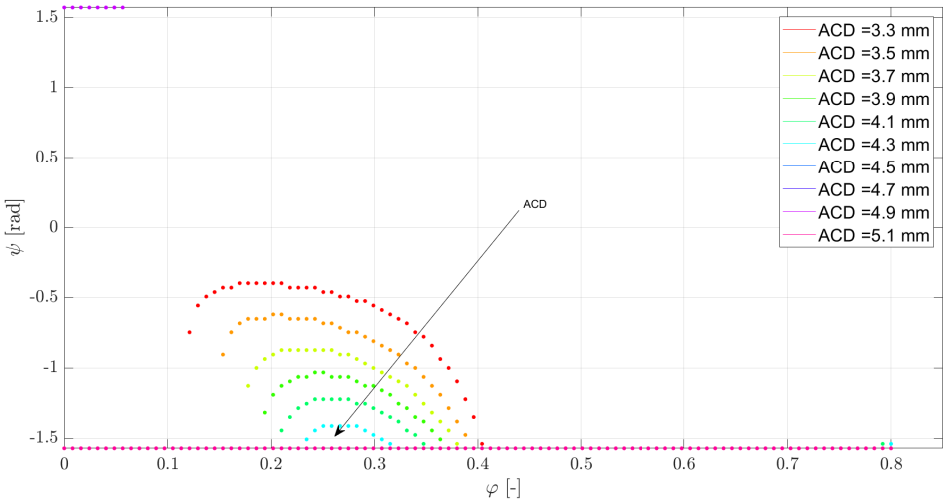

(b) Pseudophakic patients

Figure 3.9: Evolution of the maximum graft coverage trajectory with respect to the ACD. The trajectories are not shown for $\varphi > 0.8$ since they are a single pool of 100% coverage, see Figure 3.8 for example.

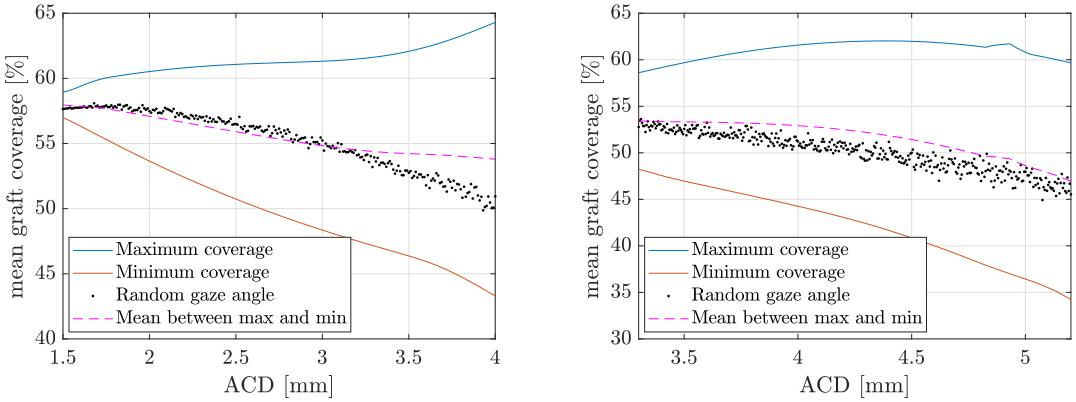

(a) Phakic patients

(b) Pseudophakic patients

Figure 3.10: Theoretical maximum and minimum mean graft coverage. In addition, the midpoint between the two is given as well as a random trajectory.

Figure 3.10a reflects two interesting phenomena for phakic patients. On the one hand, the difference between the maximum and minimum mean graft coverage is much larger as the ACD increases: around 2% for ACD = 1.5 mm and 25% for ACD = 4 mm. This supports the idea that controlling the gaze angle is crucial for large ACD while more relaxed measures can be applied to small ACD. On the other hand, applying random[2] gaze angles follows the mid-point between the maximum and minimum mean graft coverage until ACD $\approx$ 3 mm. However when ACD $>$ 3 mm, random gaze angles are worse than the mid-point. Again, emphasizing the importance of controlling the gaze angles in patients with large ACDs.

Unlike the phakic case, even *small* pseudophakic ACDs suffer a large variation of the mean graft coverage if the position of the patient is not taken care of, see Figure 3.10b. This is critical for large ACDs. A patient with a pseudophakic ACD equal to 5 mm has a maximum average coverage of 60% but a minimum of 35%. In addition, if a random position of the patient is applied this is only slightly better than the minimum, 45%. Therefore, it is again recommendable to not depart far from the maximum coverage trajectory for the patient's specific geometry. Usually achievable if the patient is always lying down face-up.

3.4.1 Considering therapeutic adherence

Some of the trajectories computed, although optimal, could be very difficult to implement with no real benefit for the patients. Two suboptimal trajectories, with low associated graft coverage deficits, are presented.

Figure 3.11 shows the theoretical maximum mean graft coverage. This optimal

[2]True random numbers are obtained from RANDOM.ORG which creates random numbers from atmospheric noise and radioactive decay.

situation is compared to the case when the patient is always lying down facing up and, a much more realistic one, the patient is lying down facing up for the first moments after the surgery –here represented until the point $\varphi = 0.5$– but then proceeds with random gaze angles (this situation is comparable to mostly being in the supine position and adding random gaze angles every certain time). All of these situations are shown as a function of the ACD.

As it can be observed, the maximum and the one where the patient is always facing up are practically the same ($\approx 5\%$ difference) for both cases. In addition, the situation where the patient is facing up until $\varphi = 0.5$ and then has random gaze angles is similar to the mid point between maximum and minimum, see Figure 3.10. The difference between the three scenarios is larger as the ACD increases. This is due to the fact that for large gas-filling ratios the variation in the gaze angle does not entail a large variation in the graft coverage, see Figure 3.4 for example. This is not the case for smaller φ, where the difference can be up to 30% depending on the position of the patient.

From a utilitarian perspective –i.e., search of the maximization of the well-being of the individuals, these conditions could be considered as good suboptimal alternatives to the maximum graft coverage trajectory. As they seek to minimize discomfort (specially since the population of patients is elderly), the rise in therapeutic adherence could increase the overall performance of the treatment.

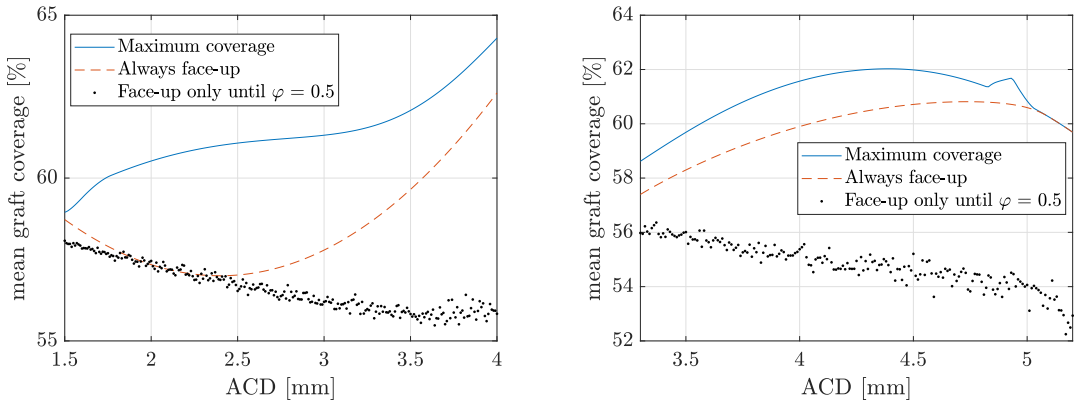

(a) Phakic patients

(b) Pseudophakic patients

Figure 3.11: Theoretical maximum mean graft coverage, mean coverage when the patient is always lying down face-up and the mean coverage when the patient is lying down face-up until $\varphi = 0.5$ but then proceeds to random gaze angles.

3.5 Heatmap

As stated in Chapter 2, it is not only important to know how much of the graft is being covered but also the areas which have been in contact with the bubble and

by which extent. This section will propose a method, initially requested by the Dr. Alberti[3], to track the projection of the bubble on the cornea along the post-operative period of DMEK.

This method will consist in introducing an arbitrary step of time –gas filling ratio, φ– and setting some probes which sense the presence of the bubble. Figure 3.12 shows a sketch of the mesh of probes on the AC used in order to sense the presence of the bubble. The example shows a 10x10 mesh, for the following simulations a 1000x1000 mesh is used in order the have a detailed map.

Initially, the gas filling ratio is set to the –maximum– one with which the patient has left the surgery. Then, it is decreased until it reaches zero, i.e., all the gas has been evacuated from the AC. With the patient-specific geometry, post-operative period and gaze angle (one per each arbitrarily small gas filling ratio) the shape, size and position of the projection of the bubble on the cornea are immediately available following the procedure exposed in Figure 3.1. At that point, the probes check if the bubble is placed on them, following Appendix C, and a counter is set. When the gas filling ratio reaches the minimum this counter is retrieved and the results are plotted in a heatmap fashion.

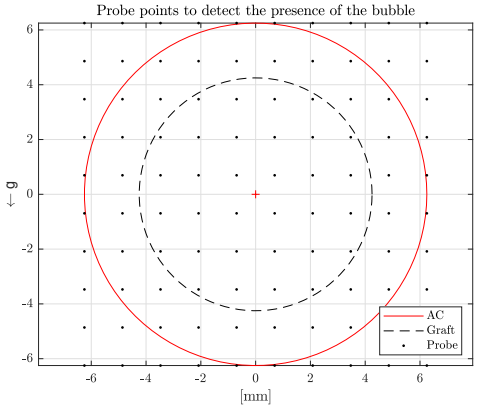

Figure 3.12: Sketch of the probes used to detect the presence of the bubble.

Figure 3.13 shows an example of the application of the heatmap to track the position of the bubble on a pseudophakic patient with an ACD = 5 mm. Regarding the gaze angles, the maximum, minimum and random graft coverage trajectories have been implemented. What was already suspected from Figure 3.10 is now graphically confirmed. The worst-case scenario of the patient's position does not only imply a 30% decrease in the time-averaged graft coverage, but it also entails areas of the graft have been barely covered during the post-op period. In addition, the random gaze angle trajectory, although it has a comparable mean coverage, displays regions with an obvious deficit in contact. Overall confirming it is critical to follow patient's positions after DMEK.

[3]Collaborator of this Thesis, from the Rigshospitalet in Glostrup, Denmark.

Two important aspects must be emphasised. On the one hand, the maximum graft coverage trajectory does not only imply maximum coverage but also a homogeneous spread. At this point, the method used in this study cannot assure this is the maximum area extend to which the bubble can pressure the graft but it can exhibit it is more even than the other trajectories studied. Figure 3.14 gives insight into why this may be, while the maximum graft coverage trajectory tends to maintain the bubble in the center of the graft (i.e., $y_c = 0$ mm) the other two situations have large vertical components of the center for large gas filling ratios. Thus, neglecting to cover the lower parts of the graft. This is critical since Gorovoy [19] found that 82% of the occurrences of peripheral donor scrolls/contractions –one of the complications after DMEK– happened in the inferior quadrants.

On the other hand, this discussion can be relaxed when talking about small phakic ACDs. As Figure 3.10 and Figure 3.11 suggested, as the ACD decreases the difference between all the scenarios is maximum of 5%, which can even be of the order of the error allowed in this research. In addition, although not shown, small phakic ACDs do not see neglected any areas of the graft. Thus, reinforcing the idea that following up with the position of the patients becomes more critical as the AC increases in size and the patients which exhibit a pseudophakic AC.

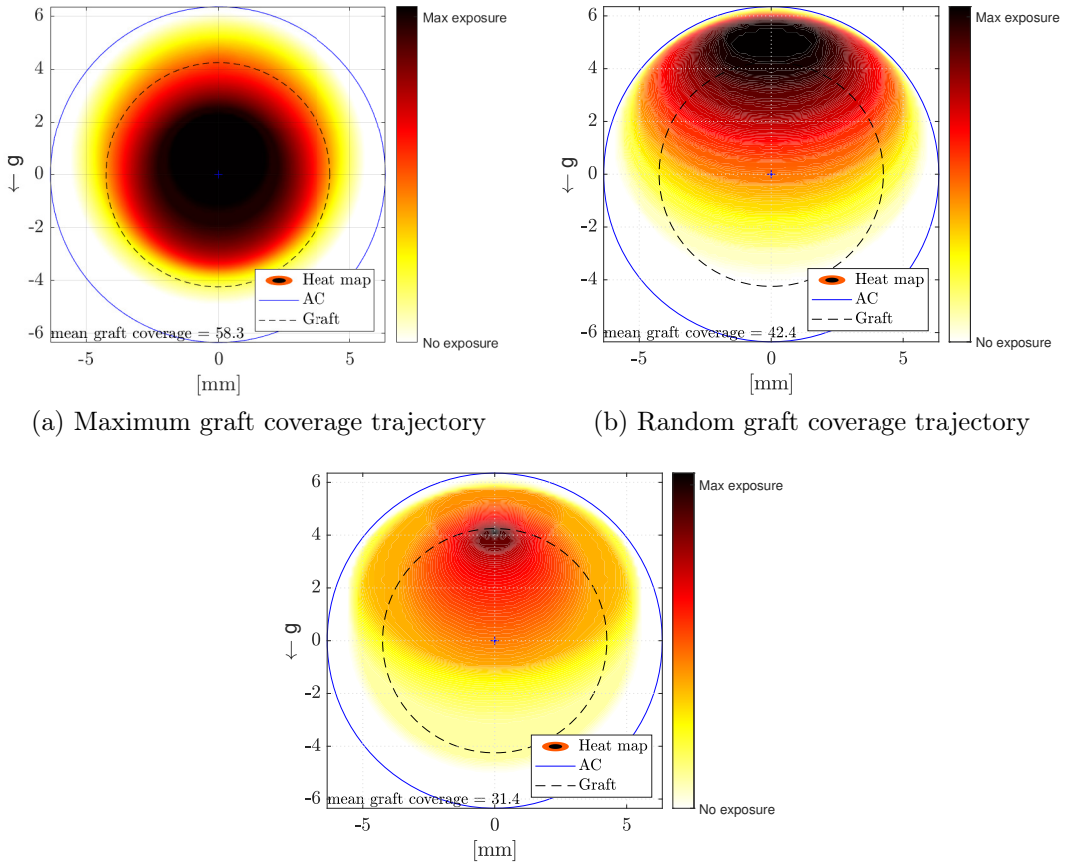

(a) Maximum graft coverage trajectory

(b) Random graft coverage trajectory

(c) Minimum graft coverage trajectory

Figure 3.13: Heatmap for ACD = 5 mm for three different post-op scenarios.

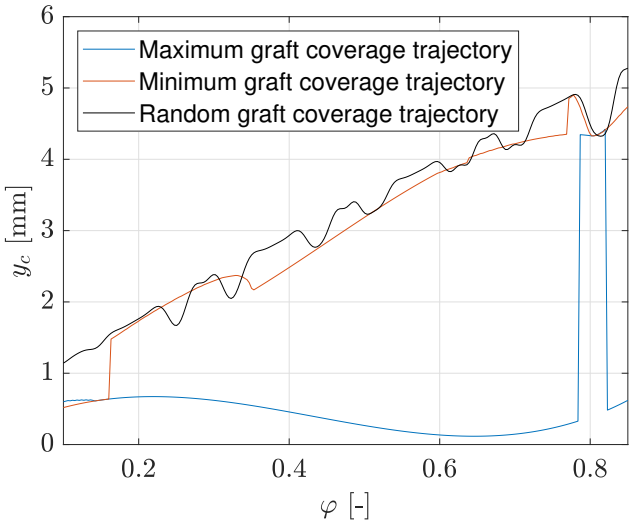

Figure 3.14: Evolution of the vertical component of the center of the projection of the bubble as the gas filling ratio decreases for a pseudophakic eye with an ACD = 5 mm, for the situations shown in Figure 3.13. The discontinuity in the maximum trajectory around $\varphi = 0.8$ can be attributed to the border where the graft coverage was artificially set to 100, see Figure 3.4.

3.6 Extension to roll

Until this point, the patient's position has been given by a single degree of freedom, the gaze angle. The pitch angle, ψ, defines if the patient is lying down facing up ($\psi = -90°$) or facing down ($\psi = +90°$), see Figure 2.6. In this section, a second rotation –roll– will be allowed around the external bilateral axis of symmetry of the patient. The roll angle, θ, represents if the patient is looking towards the left ($\theta < 0°$) or towards the right ($\theta > 0°$), see Figure 3.15.

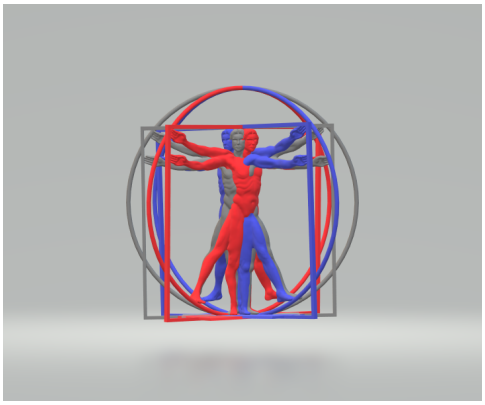

Figure 3.15: Description of the roll angle, θ: positive blue, negative red. CAD model obtained from [14].

The AC geometry will be fixed to a frame of reference and the gravitational vector will be rotated accordingly. Therefore, the generic gravity vector in the frame of reference of the AC allowing pitch and roll is:

$$\frac{g_x}{g_0} = -\cos(\psi) \tag{3.6}$$

$$\frac{g_y}{g_0} = \cos(\theta)\ \sin(\psi) \tag{3.7}$$

$$\frac{g_z}{g_0} = \sin(\psi)\ \sin(\theta) \tag{3.8}$$

Rerunning all the simulations for the roll angle as it has been done for the gaze angle would be impossible time-wise. Therefore, some kind of relationship is hoped to be drawn from the two angles, taking into account the AC is symmetrical and the equilibrium state does not depend on the initial position of the bubble.

Some considerations must be made in order to correctly compare the angles. As Figure 3.16 shows, when relating the gaze and roll angles the following equivalence must be performed

$$\psi \equiv |\theta| - 90°, \tag{3.9}$$

in addition, the solution is mirrored when $\theta > 0°$.

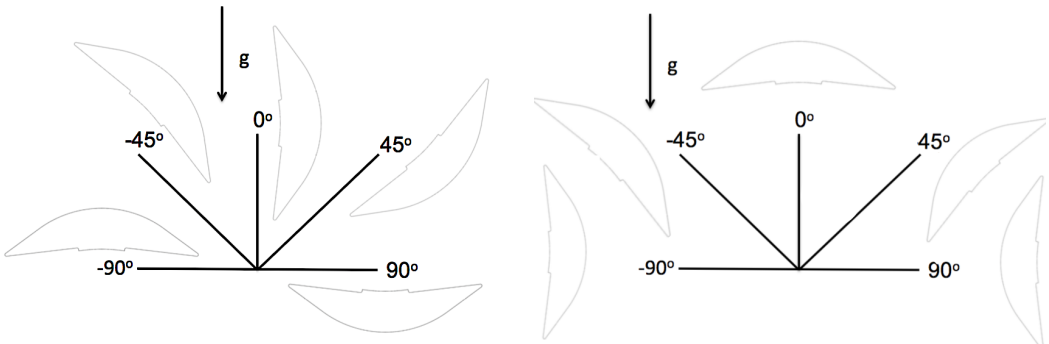

(a) Gaze angle, ψ.

(b) Roll angle, θ.

Figure 3.16: Comparison of the definitions of the gaze and roll angles.

When the pitch angle is $\psi = \pm 90°$, the solution is trivial. The center of the bubble, $\mathbf{x_c} = (x_c,\ 0)$, for a generic $\theta \in [-90°,\ 90°]$ is the solution found for the gaze angle following Equation 3.9 rotated by an angle of $\pm 90°$, depending on the sign of the roll. While the gaze angle controlled the vertical movement of the bubble, the roll angle will be in charge of providing the horizontal component.

However, this discussion becomes much more intricate when $\psi \neq \pm 90°$. Figure 3.17 shows an example of a pseudophakic case with an ACD = 5 mm, $\psi = 43°$

and $\varphi = 0.37$ when changing the value of the roll. Note that in this case $\theta = \pm 90°$ does not yield a 90 degree rotation as with the $\psi = \pm 90°$. This is due to the fact that there is a strong coupling between the pitch and roll.

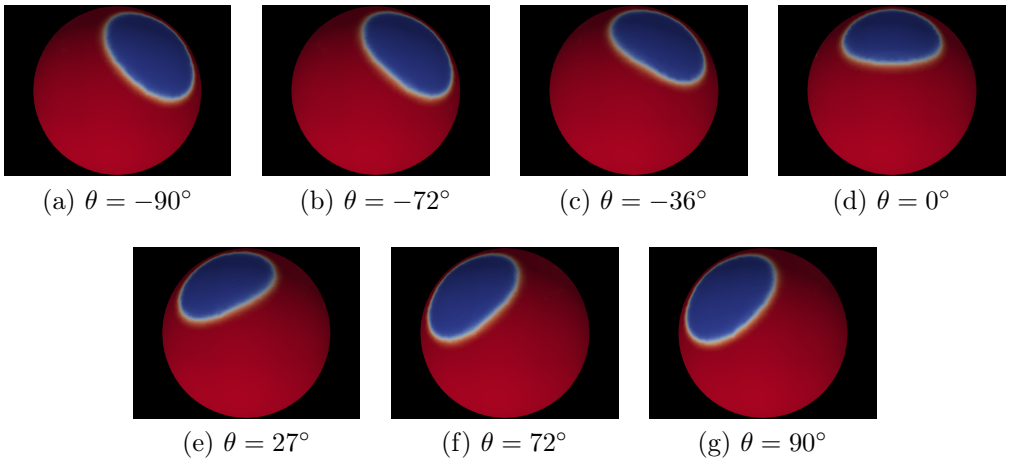

(a) $\theta = -90°$ (b) $\theta = -72°$ (c) $\theta = -36°$ (d) $\theta = 0°$

(e) $\theta = 27°$ (f) $\theta = 72°$ (g) $\theta = 90°$

Figure 3.17: Equilibrium state of the projection of the bubble on the cornea, for a pseudophakic patient with an ACD = 5 mm, a $\varphi = 0.37$ and a gaze angle $\psi = 43°$ when varying the roll angle. Red is the AH; blue, the gas; and white, the transition between both.

Due to the new degree of freedom, the center of the bubble does no longer move exclusively in the vertical axis. Thus, it is much more convenient to work in polar coordinates. It is important to note the minor axis of the ellipse is always aligned with the polar axis (i.e., the major axis is always perpendicular to the polar one), see Figure 3.17.

The angle of rotation, α, is linked to θ and ψ in an elegant manner. Figure 3.18 shows the distribution of the α [4] as a function of the roll angle, θ. Immediately, it is recognized the rotation angle follows the error function. The elegance lies in that the upper and lower bounds are exactly the gaze angle, ψ. Therefore this relation can be expressed as:

$$\alpha = \psi \operatorname{erf}(\theta), \tag{3.10}$$

where erf is the error function,

$$\operatorname{erf}(\theta) = \frac{2}{\sqrt{\pi}} \int_0^{\theta} e^{t^2} dt.$$

[4]Obtained in an heuristic way by simulating different roll angles, detecting the coordinates of the center and applying the four-quadrant inverse tangent, atan2.

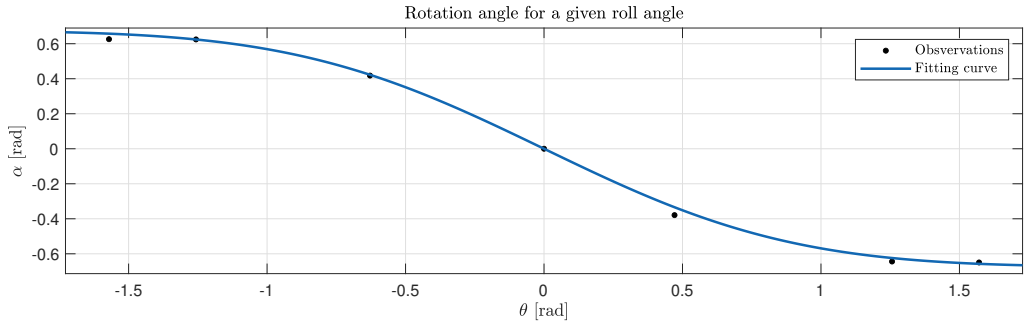

Figure 3.18: Distribution of the polar angle, α, as a function of the roll angle, θ. For a pseudophakic eye with an ACD = 5 mm, $\psi = -36°$ and $\varphi = 0.37$.

The center of the bubble is transformed into Cartesian coordinates assuming the radial coordinate for x_c is controlled by roll and the one for y_c, by pitch. Therefore, the following can be written

$$\mathbf{x_c}(\psi, \theta) = (x_c,\ y_c) = \begin{cases} x_c = -\text{sign}\,(\psi)\,\text{sign}\,(\theta)\, y_{\psi=|\theta|-90°} \cdot \sin|\alpha| \\ y_c = y_\psi \cdot \cos\alpha \end{cases} \tag{3.11}$$

where all the sign functions and absolute values take into account the mirroring of the AC as shown in Figure 3.16.

As for the size and shape of the bubble, the relationship will be approximated. When there is no rotation (i.e., $\alpha = 0°$) the bubble must only have information about the gaze angle and when there is total rotation (i.e., $\alpha = \pm 90°$) there must be exclusively information of the roll. After some trial an error of different approaches, a linear interpolation showed a good approximation of the results:

$$a\,(\psi,\,\theta) \approx \left(1 - \frac{2}{\pi}|\alpha|\right) \cdot a_\psi + \frac{2}{\pi}|\alpha| \cdot a_{\psi=|\theta|-90°} \tag{3.12}$$

$$e\,(\psi,\,\theta) \approx \left(1 - \frac{2}{\pi}|\alpha|\right) \cdot e_\psi + \frac{2}{\pi}|\alpha| \cdot e_{\psi=|\theta|-90°} \tag{3.13}$$

$$graft\,(\psi,\,\theta) \approx \left(1 - \frac{2}{\pi}|\alpha|\right) \cdot graft_\psi + \frac{2}{\pi}|\alpha| \cdot graft_{\psi=|\theta|-90°} \tag{3.14}$$

All these approximations accumulate a series of errors. They have been obtained with a limited amount of simulations (20), thus they must be handled with care. However, the observed errors are never past the millimeter in x_c, y_c, a; past 0.1 in e and 5% in the graft coverage.

3.7 Patient-specific example

As a practical application of the discussion done in this Thesis, a patient-specific heatmap will be constructed with real records of a post-operative period after DMEK.

The position of the patient as well as the AC characteristics were ceded by Alberti et al. [2]. The collection of the data set was performed as follows[5]. A small inertial measurement unit (IMU)[6] was secured to the skin of the participant's temple with hydrocolloid dressing. A shielded wire from the IMU was connected to a waterproof plastic case hung on a string placed around the patient's neck. This waterproof case contained a microcontroller[7], a microSD card data logger[8], a button to aid the calibration process, a real-time clock[9] and a lithium ion polymer battery[10] (3.7 V, 2500 mAh).

Software features of the device included logging the values from the accelerometer, gyroscope, magnetometer, temperature and pressure sensor. Logging occurred twice per second, and each measurement was stamped with a datetime value from the real-time clock. Between each logging instance, sensor values were averaged from the 400 Hz measure rate. To derive orientation from the device, an open-source sensor fusion algorithm was used to calculated unit quaternions. Then, these quaternions were transformed to Euler angles using MATLAB's `quat2eul` function in order to match the descriptions in Figure 3.16 –symmetries and mirrorings have been taken into account.

Figure 3.19 shows the evolution of the pitch and roll on a pseudophakic patient with an ACD = 3.76 mm during his or her post-operative period of 3 days ($\approx 2.6 \cdot 10^5$ seconds, see the x-axis). On the one hand, –as it can be seen in the pitch histogram– the patient's gaze angle was random, but mostly being lying down facing up and down (consistent, for example, with sleeping). The dispersion around the $\pm 90°$ can be attributed to normal movements of the head and eyes. On the other hand, the roll angle follows a Gaussian distribution around $\theta = 0°$. This is not unexpected since many random natural processes tend to have a normal distribution, mostly due to the central limit theorem (Smith [20]). Therefore, the confirmation that the roll angle is normally distributed supports the idea of exclusively controlling the patient's gaze angle.

[5] Description of the process courtesy of Dr. Alberti.
[6] MPU-9250 accelerometer, gyroscope and magnetometer; Pesky Products, Danville, CA, USA.
[7] Teensy 3.2; PJRC, Portland, OR, USA.
[8] Teensy microSD PJRC.
[9] DS3231 Precision RTC; Adafruit, New York, NY, USA.
[10] Adafruit.

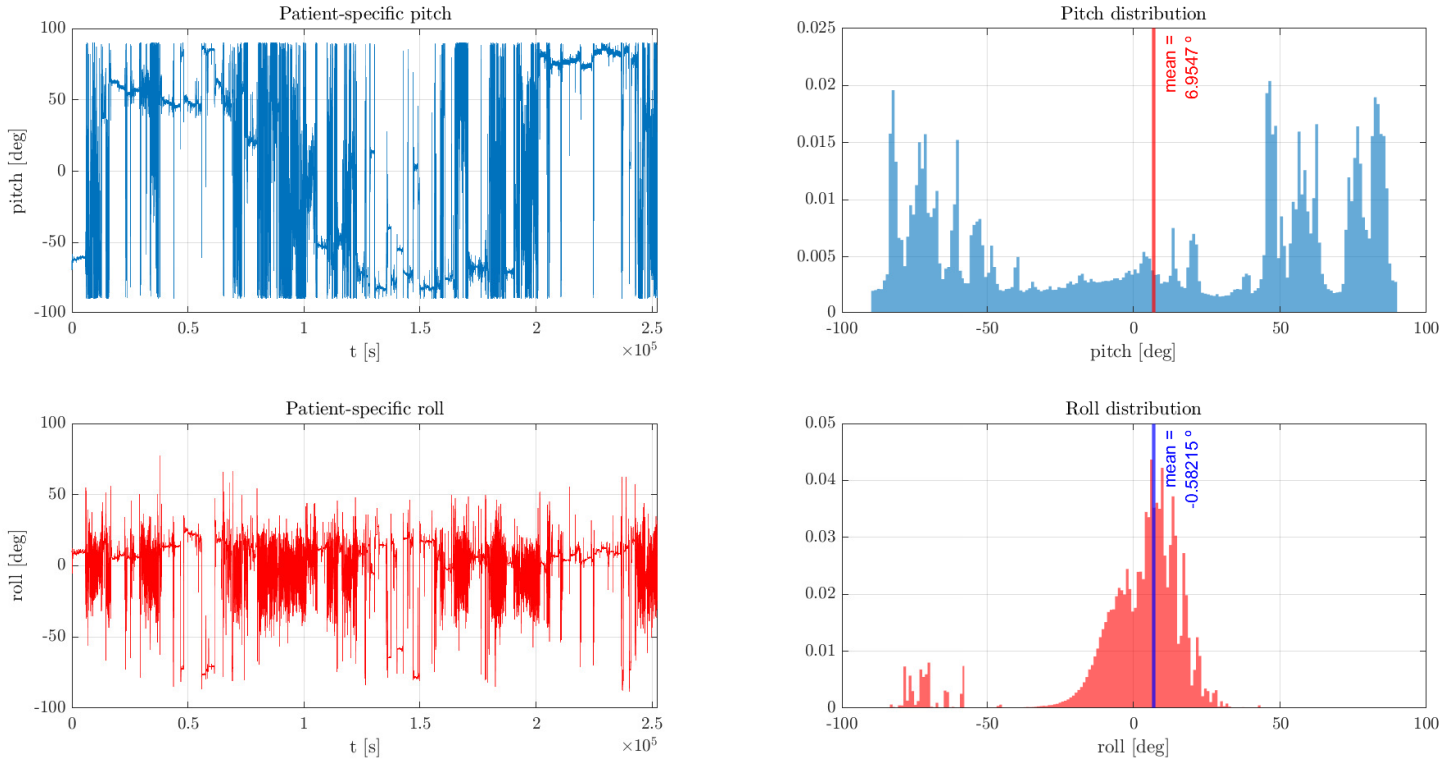

Figure 3.19: Patient-specific evolution of the pitch and roll angles, as defined in Figure 3.16.

Figure 3.20 shows the patient's specific heatmap. The mean graft coverage –over all gas-filling ratios– was 52%. As Figure 3.10 shows, a pseudophakic patient with an ACD = 3.76 mm following a random gaze angle trajectory would have a mean graft coverage of around 53%. Thus, as the histogram suggested, it is safe to say that this patient did not undergo a strict monitoring of his or her position. The coveragewise deficit s/he experienced by not following the maximum graft coverage trajectory is of about 10%.

However, the deficit on the mean graft coverage is not the most negative effect of not following the maximum graft coverage trajectory. As Section 3.5 advanced, this patient's trajectory led the bubble to fail covering the bottom quadrants. However, the insertion of the roll degree of freedom has had a favorable contribution to the homogeneity of the coverage –when comparing the same pitch angle series with and without the roll contribution. But, it has not repaired the deficit in the inferior part of the graft.

Overall, the role played by the roll is negligible to the mean graft coverage and noticeable –but not critical– to its homogeneity. Stressing the fact that controlling the pitch angle is crucial for a correct healing of the graft and that allowing the normal movement in the roll direction could be beneficial. These results suggest (and many other simulations not shown) that, as a first approximation, measuring the patient's gaze angle would be sufficient to have an idea of the contact areas.

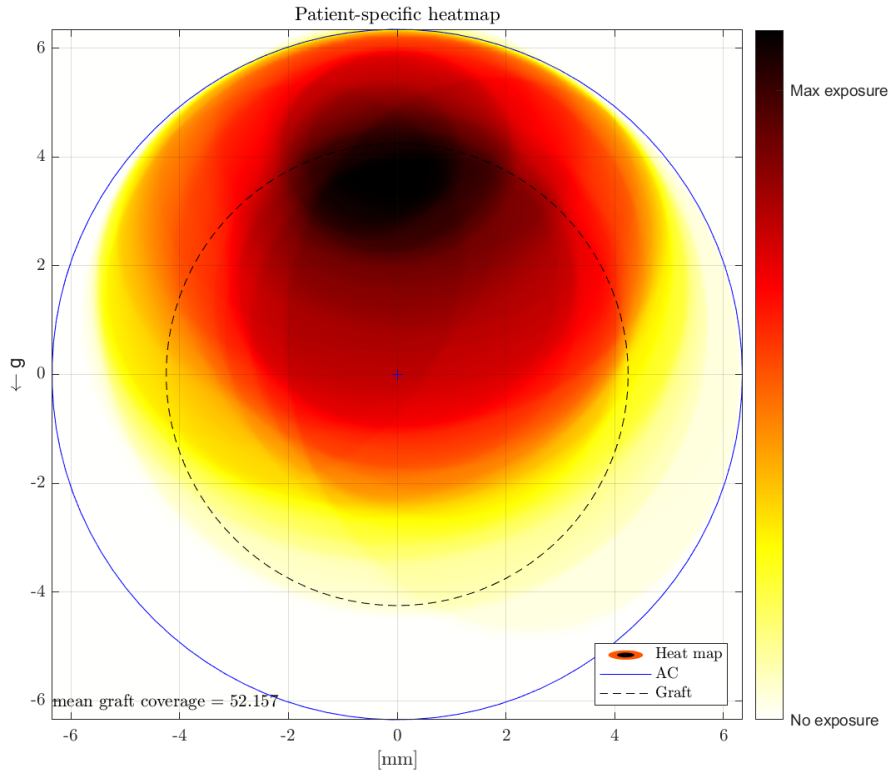

Figure 3.20: Patient-specific heatmap; pseudophakic eye with an ACD = 3.76 mm and the trajectory given by Figure 3.19.

4 | Discussion

In the current literature of DMEK, little is known about the exact behaviour of the intraocular bubble in the post-operative period although it is critical for the adherence and healing of the patient's graft. This Thesis has gone a step further on grounds of the work by Pralits et al. [1] who characterized the coverage of the graft for a single degree of freedom and some discrete ACDs.

The shape, the size and the position of the projection of the bubble on the cornea have been completely characterized for phackic and pseudophakic patients throughout all their post-op period by a set of simple coefficients, given in Appendix B, for the two most important degrees of freedom of the patient, roll and pitch. The coverage of the graft ($S_{\text{air}}/S_{\text{graft}}$) has also been determined on these bases. The validity of these results has not been determined clinically but a numerical cross-validation was performed confirming their reliability at least in the range of ACDs and gas filling ratios of the eligible patients for DMEK in Alberti et al. [2].

It has been shown that for small ACDs –especially in phakic eyes– the ability of the surgeon to inject the correct amount of gas dominates over what the patient can do with his or her position. A phakic eye with an ACD = 1.8 mm suffers variations of around 5% when the gaze angle is changed but every 10% decrease in the gas filling ratio means the graft coverage also decreases 10%, see Figure 3.2. However, as the ACD increases –especially in pseudophakic patients– the position gains dominance over the gas filling ratio. For example, a pseudophakic eye with an ACD = 5.2 mm with a $\varphi = 0.4$ can have half of the graft covered when lying down facing up but no coverage at all when facing down, see Figure 3.4. This same eye, will also experience 50% variations on the graft coverage when decreasing the gas filling ratio 10% if the placement of the AC is not optimal. However, this 10% reduction in φ can also only imply a 10% variation in the coverage, as in the small phakic eyes, if the patient's position is correct. Thus, as the ACD increases it is crucial to monitor the patient's position carefully while more relaxed measures seem to be sufficient for small ACDs, especially in phakic eyes.

The large variations on the graft coverage as the ACD increased have been explained by the phenomenon here called *bubble detachment*. This process implies that as the patient rotates towards the face down position, the bubble will be placed on the lens and iris and it will not contact the graft. This procedure has been deter-

mined by two simple conditions on the numerical model proposed in this Thesis. A geometrical limitation on DMEK has been given: if the ACD > 6 mm large regions in the $\varphi - \psi$ space are not covered by the bubble limiting the application of this procedure. However, the possibility of a patient presenting these sizes of the AC is very improbable. Nevertheless, it has been shown that large ACDs –especially pseudophakic– have areas below $\varphi = 0.5$ which imply no coverage of the graft for many or all gaze angles. For example, these patients can exhibit this phenomenon while walking (i.e., horizontal gaze, $\psi = 0°$) for $\varphi < 0.3$.

As the gaze angle can be easily modified by healthcare personnel by inclining the patient's bed, the position has been optimized for this degree of freedom. A trajectory of maximum graft coverage has been given which yields the optimal gaze angle for every gas filling ratio, given an AC geometry. When compared to the worst-case scenario, the difference of using or not this trajectory is minimal for small ACDs –especially in phakic cases. However, the differences can become significant as the ACD increases –especially in pseudophakic eyes. Following the maximum graft coverage trajectory can imply an overall 35% increase in the time-average graft coverage over all the post-op period.

Different medical phenomena after DMEK, such as graft detachment, justify the need of characterizing the position of the bubble as well. It has been observed that the maximum graft coverage trajectory not only yields optimal contact but also implies a homogeneous graft coverage. As the ACD increases –especially in pseudophakic patients– the bubble tends to be in the superior half of the AC. This causes a deficit in coverage in the lower half of the AC, see Figure 3.13. The Gaussian distribution of the roll angle –caused by the normal movements of the patient in the bed– has been shown to slightly increase the graft coverage but most importantly it somewhat spreads-out the contact surface of the bubble. However, the roll angle has not been optimized thus this is only a preliminary insight. In summary, controlling the patient's pitch –especially as the ACD increases– is crucial in order to have both a high mean graft coverage and a homogeneous contact. At first instance, it seems correct to allow the normal movement of the patient in the roll axis as it evens out the covered area without hindering the percentage of the graft been covered.

Many of the maximum graft coverage trajectories are uncomfortable to follow. Therefore, from a utilitarian perspective, suboptaimal alternatives are proposed. As they seek to minimize discomfort (especially since the population of patients is elderly), the rise in therapeutic adherence could increase the overall performance of the treatment. It was found that always lying down facing up was a good compromise between very strict following of the patient's gaze angle –maximum trajectory– and no restrictions at all –random– as it yielded a homogeneous coverage with only a 5% difference in the mean coverage with respect to the theoretical maximum achievable.

As a product of this Thesis, the results are available in different forms for their clinical use. A priori formats have been given such as contour graphs, time-averages and tables so that medical personnel can have an insight about the consequences of certain positions of their patients' graft coverage after DMEK. A posteriori designs

are also proposed such as heatmaps which can be used to characterize certain phenomena observed in patients after the healing process is over with respect to the mean behavior of the bubble in the post-op period.

As an unexpected result of the numerical sensitivity analysis, a suggestion can be made to medical researchers studying DMEK. The model proposed in this Thesis has found the equilibrium state seems to be robust to changes in the contact angle at the iris while very sensible to the one at the cornea. Therefore, refining the measurement of the contact angle at the cornea seems much more critical than exhausting resources in order to obtain novel quantities for the iris, as to date no clinical trials have studied this quantity.

All the results discussed in this document are restricted by two fronts. On the one hand, the geometries are extreme simplifications of the real behavior of the AC. A rigid chamber has been considered instead of the real flexible one with moving boundaries. After DMEK, drugs and the gas bubble affect the iris shape and, therefore, the shape of the AC. This is especially true in pseudophakic eyes where extraction of the lens leaves ample room for iris mobility, Pralits et al. [1]. On the other hand, simplicity on the interpolation of the results was imposed over the quality –as they needed to be understandable to a non-engineering audience. Thus, the method shown in the flowchart in Figure 3.1 and the simplifications on the roll angle give rise to a series of error which cannot be dismissed. Numerical cross-validation of these results have been performed assessing their validity but to date no clinical comparisons have been done.

4.1 Future work

Due to deadline restrictions some topics have been left unresolved for future students to tackle. Here a non-exhaustive list is proposed:

- The interpolation of the results of the roll angle have been done with a limited amount of numerical observations. Therefore, a more careful analysis could be performed.

- A third degree of freedom could be studied. The IMU discussed in Section 3.7 yields a yaw angle which determines if the patient's head is above or below his or her center of mass. Thus, the problems on the coverage of the lower half of the graft could be possibly solved exploiting this third angle.

- The maximum graft coverage trajectory points towards a homogeneous spread of the graft coverage, but in general it does not need to be necessarily the most homogeneous. Therefore a second optimization problem could be proposed which tackles this aspect, maybe introducing the roll angle to the picture.

- The diameter of the AC has been considered constant, but studies such as Savini et al. [17] have found variations depending on the patient. It is another possible research path.
- Different suboptimal post-operative scenarios could be more deeply discussed with doctors in order to have real insight about the behaviors of the bubble considering real patient conducts after DMEK.
- Other result formats could be introduced, focusing in the creation of simple computer softwares with which doctors could interact.
- ...

Appendices

A | International Collaboration for a Master Thesis

This section aims to explain –in a more personal note– how this Thesis has been carried out and to encourage future *tesisti* to consider this option. In addition, by lying down my personal experience I hope to help teachers in the new future ahead of us.

I am a Spanish student, currently studying in Politecnico di Milano. After discussing with Professor Quadrio about the possibility of conducting my Thesis with him –as I was interested in biofluids– he referred me to Professor Pralits' research in the Universtà degli Studi di Genova. He was looking for a student to help him with some CFD simulations regarding the research he was conducting in collaboration with Dr. Alberti from the Rigshospitalet (Glostrup, Denmark). Thus, it was the perfect opportunity for me: an interesting international experience regarding a topic I was interested in.

As I was still living in Milan and I had no intention of moving to Genoa, the initial idea was to: set up periodic online meetings with Professor Pralits, send him weekly or biweekly reports of my work and travel to Genoa as many times as possible. Then, every month we had a meeting with Dr. Alberti to get his feedback, help us define better the objectives and refine the results. In fact, by the 1st of March, I had travelled to Genoa twice. It is a very quick and easy 2-hour train ride from Milan's Stazione Centrale to Genoa's Brignole, right next to the University. I would invite anyone in Italy to follow this method. For my colleagues at Polimi, I believe any city north of Bologna would be feasible in this style.

However, for those readers of the future, this is being written in June 2020. In March 2020, Europe (especially in the beginning, Lombardia) was hit with the Covid-19 pandemic and de facto all international students were advised to go back home by their countries. Currently in June 2020, Majorca (Spain) –the island I grew up in and where I have been since March– is now entering the so called Phase 3 towards "new normality". For the whole months of March and April, stay-in-home orders were enforced. Thus, the strategy had to be slightly changed.

The final approach was defined right after. We decided to send weekly reports to Professor Pralits where in 10 pages I would inform him of that week's work and

most interesting results and conclusions. Then, 2 or 3 days later he would answer me back with the same document with comments. Every 2 or 3 weeks this would be complemented by an online meeting where objectives were set and paths were redefined. Every month, I would set up a presentation to show the doctor my results and vary them as he thought was most useful for his research. I believe this method has worked very well and no great inconveniences were encountered.

I actively promote all students to consider this alternative of heavy international collaboration, especially in the times that are coming were face-to-face meetings will no longer a priority.

B | Interpolation of the results: Matrices of coefficients

This appendix contains the value of the coefficients for the interpolation of the results as shown in Equation 3.3 following Figure 3.1. The coefficients are given for the ACD in millimeters, the gaze angle in radians and the gas filling ratio in mL/mL. The matrices have been formatted from MATLAB using `matrix2latexmatrix`[1].

B.1 Phakic patients

The coefficients for the semi-major axis are:

$$A_a = \begin{pmatrix} -4.4957 & 22.6639 & -25.6307 \\ 7.929 & -40.1493 & 45.5061 \\ -4.3676 & 22.4396 & -25.6317 \\ 0.72385 & -3.8847 & 4.5417 \\ -4.0056 & 20.9499 & -23.3934 \\ 6.8418 & -35.3625 & 39.3165 \\ -3.7844 & 19.6424 & -21.9988 \\ 0.69064 & -3.8168 & 4.4559 \\ 9.2833 & -47.6702 & 54.7995 \\ -16.1862 & 83.1056 & -95.514 \\ 8.77 & -45.3854 & 52.3844 \\ -1.4114 & 7.5628 & -8.8952 \\ 1.4621 & -6.9729 & 7.515 \\ -3.6821 & 16.2852 & -18.2068 \\ 2.9512 & -13.4201 & 20.8613 \\ -0.58657 & 3.319 & -3.3722 \end{pmatrix}$$

for the eccentricity:

[1] nicolamr Marcacci Rossi (2020). Matrix to latex Matrix (https://www.mathworks.com/matlabcentral/fileexchange/28880-matrix-to-latex-matrix), MATLAB Central File Exchange. Retrieved June 7, 2020.

$$A_e = \begin{pmatrix} 0.60662 & -4.3265 & 5.8008 \\ -0.80376 & 5.9754 & -8.1206 \\ 0.33983 & -2.5922 & 3.5511 \\ -0.027001 & 0.2326 & -0.32984 \\ -5.0449 & 25.8034 & -30.0238 \\ 7.0243 & -35.669 & 41.3408 \\ -2.9515 & 14.9501 & -17.304 \\ 0.4367 & -2.3431 & 2.7949 \\ -0.12293 & 2.8132 & -4.6418 \\ -0.14635 & -2.5259 & 4.9903 \\ 0.21152 & 0.30184 & -1.218 \\ -0.071278 & 0.30889 & -0.32452 \\ 0.37599 & -2.4361 & 3.1559 \\ 0.43172 & -2.2313 & 2.6108 \\ -0.3152 & 1.6686 & -1.9769 \\ -0.25387 & 1.8314 & -2.4647 \end{pmatrix}$$

for the vertical position of the center of the projection of the bubble with respect to the center of the AC:

$$A_y = \begin{pmatrix} -1.775 & 5.7269 & -2.6723 \\ 2.49 & -7.2859 & 2.0907 \\ -1.4897 & 4.6809 & -1.9737 \\ 0.46264 & -1.7974 & 1.3693 \\ -7.0219 & 38.0966 & -45.0376 \\ 12.286 & -67.1725 & 80.638 \\ -7.1332 & 39.5832 & -47.4388 \\ 1.4826 & -8.4649 & 9.6521 \\ 1.9718 & -5.9173 & 1.3706 \\ -2.183 & 3.5269 & 5.6619 \\ 1.0566 & -1.3105 & -4.1252 \\ -0.3515 & 1.318 & -0.4507 \\ -0.72464 & 4.2663 & -15.1714 \\ -0.77737 & 3.2317 & 11.2963 \\ 2.2763 & -13.9689 & 10.02 \\ -0.81423 & 6.2794 & -5.987 \end{pmatrix}$$

and finally, the coefficients for the percentage of the graft being covered:

$$A_{\text{graft}} = \begin{pmatrix} 34.2233 & -139.8716 & 138.9195 \\ -39.2411 & 151.9601 & -147.7025 \\ 9.6461 & -30.0578 & 26.5867 \\ 0.10392 & -2.1643 & 2.4851 \\ 132.3486 & -743.6037 & 797.6004 \\ -184.6316 & 1029.3654 & -1098.3527 \\ 68.0274 & -374.6796 & 396.2442 \\ -3.9922 & 22.7474 & -23.6422 \\ -43.5272 & 192.1651 & -185.2736 \\ 49.207 & -191.757 & 165.5344 \\ -11.9133 & 26.9177 & -7.0192 \\ -1.311 & 8.9358 & -11.4442 \\ -88.1701 & 645.2676 & -1083.1294 \\ 107.3539 & -783.0893 & 1327.5624 \\ -30.2052 & 219.3917 & -254.9243 \\ -1.5198 & 2.2653 & 1.3481 \end{pmatrix}$$

B.2 Pseudophakic patients

The coefficients for the semi-major axis are:

$$A_a = \begin{pmatrix} -11.4663 & 88.9511 & -169.5722 \\ 18.9891 & -147.851 & 282.3823 \\ -9.6274 & 75.6592 & -145.2087 \\ 1.4197 & -11.4662 & 22.3013 \\ -8.5625 & 63.2169 & -112.7531 \\ 15.2833 & -114.4568 & 208.4672 \\ -8.2002 & 62.5439 & -116.1291 \\ 1.1177 & -8.8145 & 16.4392 \\ 10.1167 & -77.1913 & 144.7363 \\ -16.2028 & 123.4515 & -230.9211 \\ 8.2371 & -63.069 & 118.2135 \\ -1.436 & 11.3105 & -21.5797 \\ 3.5918 & -24.1405 & 38.2161 \\ -5.3491 & 34.6112 & -55.8632 \\ 2.7061 & -17.5237 & 35.2513 \\ -0.66726 & 5.1082 & -8.4418 \end{pmatrix}$$

for the eccentricity:

$$A_e = \begin{pmatrix} 0.22708 & -3.2708 & 9.8962 \\ 0.046918 & 1.6635 & -8.4455 \\ -0.48926 & 3.2223 & -4.3606 \\ 0.25508 & -2.0518 & 3.963 \\ -6.4608 & 53.4821 & -106.807 \\ 9.0487 & -74.6757 & 148.7153 \\ -3.7406 & 30.7503 & -60.9882 \\ 0.48698 & -3.9875 & 7.7084 \\ 1.6076 & -12.53 & 23.3829 \\ -3.4844 & 27.9877 & -54.1012 \\ 2.3853 & -19.6169 & 38.9614 \\ -0.44565 & 3.7294 & -7.4387 \\ 2.7757 & -23.5061 & 46.2568 \\ -4.1083 & 34.6146 & -68.528 \\ 1.5768 & -13.2341 & 26.0186 \\ 0.066573 & -0.58608 & 2.1884 \end{pmatrix}$$

for the vertical position of the center of the projection of the bubble with respect to the center of the AC:

$$A_y = \begin{pmatrix} 0.0269 & 4.2092 & -10.3009 \\ -0.43862 & -3.7826 & 12.0284 \\ 0.92949 & -3.0608 & 1.1614 \\ -0.41947 & 2.4038 & -2.9406 \\ 7.4597 & -40.4091 & 49.9302 \\ -11.8882 & 65.2593 & -82.0155 \\ 6.3293 & -35.7459 & 48.1456 \\ -1.2285 & 7.2641 & -11.4617 \\ 4.3442 & -27.1055 & 39.1217 \\ -6.6045 & 40.5821 & -58.6581 \\ 2.6834 & -15.9504 & 22.5029 \\ -0.27273 & 1.4298 & -1.4423 \\ -5.254 & 30.0537 & -40.5908 \\ 7.4362 & -43.0946 & 58.7408 \\ -2.9674 & 17.3293 & -28.9776 \\ 0.24503 & -1.1994 & 6.9043 \end{pmatrix}$$

and finally, the coefficients for the percentage of the graft being covered:

$$A_{\text{graft}} = \begin{pmatrix} -118.8352 & 974.5108 & -1908.9791 \\ 183.3799 & -1494.2221 & 2915.575 \\ -83.776 & 678.4248 & -1318.1727 \\ 9.7741 & -79.2022 & 153.9643 \\ -40.2344 & 318.4948 & -791.9438 \\ 85.6508 & -669.3271 & 1528.3114 \\ -49.527 & 380.4654 & -806.8408 \\ 5.6393 & -41.0377 & 80.6098 \\ 57.0791 & -489.0533 & 973.4736 \\ -94.2227 & 814.1598 & -1616.7128 \\ 47.2771 & -412.2613 & 817.8252 \\ -5.1207 & 43.2047 & -85.222 \\ -19.393 & 193.9563 & -368.0897 \\ 15.2957 & -167.5891 & 328.3427 \\ -5.1151 & 56.0796 & -6.1011 \\ 1.6975 & -19.3236 & 41.169 \end{pmatrix}$$

C | Detection of the bubble for the heatmap

From the information retrieved from Figure 3.1, the projection of the bubble must be reconstructed for every gas filling ratio and gaze angle. This appendix will propose a method for this reassemble for a generic rotated non-centered ellipse. These conic sections follow:

$$A(x - x_c)^2 + 2B(x - x_c)(y - y_c) + C(y - y_c)^2 = 1.$$

In linear algebra, conic sections are usually represented in a matrix fashion as:

$$(x - x_c \;\; y - y_c) \begin{pmatrix} A & B \\ B & C \end{pmatrix} \begin{pmatrix} x - x_c \\ y - y_c \end{pmatrix} = 1,$$

where the central matrix is normally called "matrix of the quadratic form", M.

With the information of the matrix of eigenvalues of M,

$$D = \text{eig}\,(M) = \begin{pmatrix} \frac{1}{a^2} & 0 \\ 0 & \frac{1}{b^2} \end{pmatrix},$$

where a and b are the semi-major and semi-minor axes, and the information of the matrix of eigenvectors (also known as the rotation matrix of the ellipse)

$$R = \begin{pmatrix} \cos\beta & -\sin\beta \\ \sin\beta & \cos\beta \end{pmatrix},$$

where β is the angle rotated by the ellipse measured from the x-axis, the equation of the ellipse can be retrieved.

These two matrices are known from the ellipse detection algorithm. The rotation angle β is, since the major axis is perpendicular to the polar one as shown in Section 3.6,

$$\beta = \text{atan2}(y_c, x_c) - \frac{\pi}{2}.$$

where atan2 is the four-quadrant inverse tangent. From these two matrices, the unknown M can be reconstructed as:

$$M = RDR^{-1},$$

since the roation matrix, R, is orthogonal $R^{-1} = R^T$,

$$M = RDR^T.$$

With the information of M, the equation of the ellipse can be rewritten. Thus, the bubble will be on top of a generic probe if

$$A(x_i - x_c)^2 + 2B(x_i - x_c)(y_j - y_c) + C(y_j - y_c)^2 \leq 1.$$

where x_i and y_j are the coordinates of the $\left(\text{i}^{\text{th}},\ \text{j}^{\text{th}}\right)$ probe of the mesh in Figure 3.12.

D | Cross-validation through machine learning

This by no mean must exit the boundaries of this document, since Machine Learning is still a very sensible area in medicine. As Professor Quadrio pointed out, predictive algorithms are able to predict *things* without explaining why they happen. Since clinical decisions taken by medical doctors must be based on true knowledge and very often need to be defended in court, the scenario of a doctor telling a judge s/he took a decision because a black box –the machine learning– told him or her is still very unrealistic. However, for the sake of this student's curiosity this section will attempt to apply a Data Science Project using Machine Learning[1].

D.1 Structure of a Data Science Project

The basic structure of any data science project is divided into five different stages:

1. Question
2. Exploratory Data Analysis (EDA)
3. Formal Modelling
4. Interpretation
5. Communication
6. Decision

Points 1 through 3 are conducted by Professor Pralits and this *tesisti*, 4 and 5 are done in collaboration with Dr. Alberti and 6 is exclusively carried out by Dr. Alberti.

[1] All this project is based on the documentation in MATLAB. No previous knowledge about Machine Learning was assumed.

D.1.1 Question

The most critical point of the whole analysis is to come up with the correct question since it will automatically define the type of data needed, the modelling necessary and the expected output. It is helpful to consider the different types of questions that exist. The six broad categories into which they can fall, as described by Leek et al. [21], are:

- **Descriptive:** It seeks to summarize the characteristics of a set of data.
- **Exploratory:** The data is analyzed in order to see if there are patterns, trends, or relationships between variables.
- **Inferential:** It is a restatement of the proposed hypothesis as a question and answering it by analyzing a different set of data.
- **Predictive:** It uses a subset of measurements (the features) to predict another measurement (the outcome) on a single unit.
- **Casual:** Seeks to find out what happens to one measurement on average if you make another measurement change. Such an analysis identifies both the magnitude and direction of relationships between variables on average.
- **Mechanistic:** Wants to show that changing one measurement always and exclusively leads to a specific, deterministic, behavior in another.

Thus, it seems quite obvious that the question regarding this Thesis is predictive. An interesting feature of standard predictive data analyses is that they only show that you can predict one measurement from another; they do not necessarily explain why that choice of prediction works. Feature which makes this kind of studies still dangerous in medical applications. However, the underlying fluid-mechanical reasons of the outcome are known. The scope, then, is the removal the CFD barrier in order to have quick and reliable predictions of the bubble's dynamics. Thus, the question proposed is:

"*Given a patient's eye geometry, his or her position and post-op period, what is the most likely position, shape and size of the bubble and the percentage of the graft which is covered by it?*"

D.1.2 Exploratory Data Analysis

In this section the data set is established. Once it created it must be broadly examined in order to check if: i) is the data correct, ii) is the data sufficient in order to answer the question, iii) does the data answer the question or does the question

need to be reformulated. Once this checklist is fulfilled, a sketch of the solution must be done in order the know –broadly– if a solution does indeed exist and how it may be.

The data set for this project has been covered broadly in this document: 179 simulations have been run for the phakic eye and a 183 for the pseudophakic. Then, in Section 3.1 it was shown that the output could be related to the features by a simple polynomial fit. Therefore confirming that the solution was indeed possible, it existed and the data was able to answer the question.

D.1.3 Formal modelling

Once the data set has been collected it is necessary to create a model which correctly predicts the outcome for unknown data.

In the previous sections a model was proposed by progressively fitting polynomials to the features. Finally obtaining a 16x3 matrix which completely defined the solution given the state of the features, see Section 3.1. In this section an alternative model is proposed to validate the previous results. Therefore, the `Regression Learner` of MATLAB will be applied to the 179 observations of the phakic case. The data consists in three features: ACD, gas filling ratio (φ) and gaze angle (ψ). The output are four: semi-major axis (a), eccentricity (e), position of the center of the bubble (y) and graft coverage (graft).

The common workflow for training regression models in the `Regression Learner` of MATLAB is shown in Figure D.1.

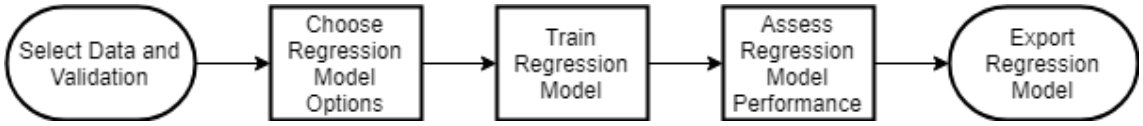

Figure D.1: Common workflow for the regression models in the `Regression Learner` of MATLAB. Retrieved from the Regression Learner Documentation.

Due to the small set of data, all training models can be tried. Once they are done, the validation results can be compared and then choose the model that performs the best for the specific regression problem. Then, this model can be used to make predictions.

In a prediction problem, the model is usually given by a data set of known data on which the model is trained with (*training set*) and a data set of unknown data against which the model is tested (*testing set*). This is called cross-validation, which tests the model's ability to predict new data that was not used in estimating it in order to look for problems like overfitting or selection bias.

The cross-validation technique normally used when only one data set is available and obtaining new unseen data is very costly (like in this CFD case) is the k-fold cross-validation. In this method, the data are randomly partitioned to form k disjoint subsets (folds) of approximately equal size. In the i^{th} fold of the cross-validation procedure, the i^{th} subset is used to estimate the generalisation performance of a model trained on the remaining $k-1$ subsets. The average of the generalisation performance observed over all k folds provides an estimate (with a slightly pessimistic bias) of the generalisation performance of a model trained on the entire sample, Cawley et al. [22]. Since this data set is so small, many folds can be performed (even the extreme case where each subset contains a single observation, which is known as leave-one-out cross-validation). See Figure D.2 for an example of a 3-fold cross-validation.

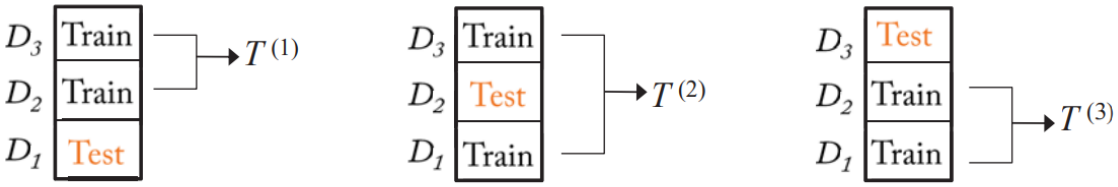

Figure D.2: Example of a 3-fold cross-validation. The original data set D is randomly split into k=3 groups D_1, D_2 and D_3. k-1=2 of the groups are allocated to the training set an the remaining one for the testing set. This process is repeated k=3 times. Retrieved from Seni et al. [23].

As stated before, all training techniques can be tried and later on compared to one and other. Using a 50-fold cross-validation, the model which performs the best for each value is:

- **Graft coverage:** `Gaussian process regression (GPR)` with a Matern kernel function with parameter 5/2 (Rasmussen [24]).
- **Semi-major axis:** `Gaussian process regression (GPR)` with squared exponential kernel function (ibid.)
- **Position of the center:** `Gaussian process regression (GPR)` with a Matern kernel function with parameter 5/2 (ibid.).
- **Eccentricity:** `Ensemble Boosted Trees` (see MATLAB's documentation).

As shown in Table D.1 the Regression Learner performed very accurately across all the values. The graft coverage can be estimated with an root-mean-square error (RMSE) of 1.14%; the semi-major axis, with 0.12 mm; the eccentricity, by 0.05; and the position of the center by 0.17 mm. All estimations are barely perfect and more than acceptable for the scope of this Thesis.

Table D.1: The models' statistics for each value computed with the validation set.

	graft [%]	a [mm]	e [-]	y [mm]
RMSE	1.140	0.118	0.057	0.167
R-squared	1.000	0.990	0.960	0.980
MSE	1.299	0.014	0.003	0.028
MAE	0.609	0.061	0.036	0.089

Figure D.3 shows for each observed value the prediction made, independently of its features. The blue dots represent the observation-prediction pair and the black line the perfect-case scenario (i.e., the predictions match the observations). The graft coverage, the semi-major axis and the position of the center are correctly captured. This is represented by a small –and symmetrical– scattering from the black best-case scenario line. Figure D.3d shows a larger scattering from the perfect prediction for the eccentricity. Thus, the eccentricity is more poorly captured by the model which can indicate the polynomial fit is also less reliable in this feature. This can be easily attributed to the ellipse detection algorithm. Being a image recognition code, the solutions it yields are not perfect. Therefore, although the size of the bubble can be correctly captured, its shape may not be very accurate. However, two ellipses with the same semi-major axis which differ by a small fraction in the eccentricity are practically the same. Thus, this small discrepancy will be allowed.

D.2 Comparison of results

As stated in the introduction, this Machine Learning model will serve as a validation for the results obtained by the fitting-coefficients model. The procedure is going to be as follows: a random trio of features is going to be inputted into both the fitting-based model and the Regression Learner model. Then, the outputs will be compared. Table D.2 shows the 10 random trios used.

Figure D.4 plots the comparision between the results when using the Regression Learner and the polynomial fit. The blue crosses are the pair of results

```
(fitting model, Regression Learner model)
```

and the black line is the perfect prediction, i.e. when the fitting model yields the same results as the `Regression Learner` one.

As it can be seen in Figure D.4, the graft coverage, semi-major axis and position of the center almost perfectly match. However, the eccentricity varies a lot, much

more noticeable when $e < 0.3$. Nevertheless, the eccentricity only affects the shape of the bubble ($b = a\sqrt{1-e^2}$) which, ultimately, only affects the heat map. The heat map itself is an approximate plot, thus it is not very important to refine this value. Therefore, it can be concluded –at least numerically– that the simple fitting coefficient model is consistent and yields reasonable results.

Table D.2: Randomly obtained trios of features.

Model number	**ACD [mm]**	φ **[-]**	ψ **[rad]**
1	2.0400	0.2284	-1.2298
2	2.2443	0.9848	-0.6780
3	2.0213	0.5915	-1.0255
4	3.6633	0.5727	-1.3134
5	1.8174	0.0644	-1.3410
6	2.1653	0.2872	1.1460
7	2.6641	0.7225	0.1604
8	1.9146	0.1713	0.4472
9	2.3827	0.0997	0.0529
10	3.5956	0.2446	1.4509

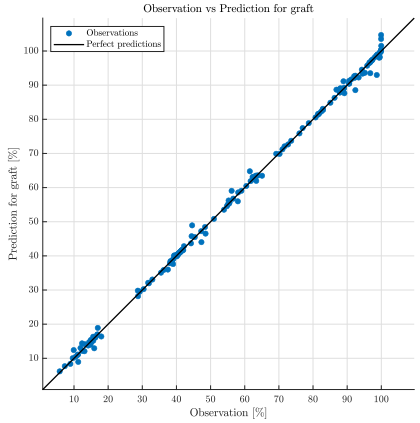

(a) Predictions for graft coverage.

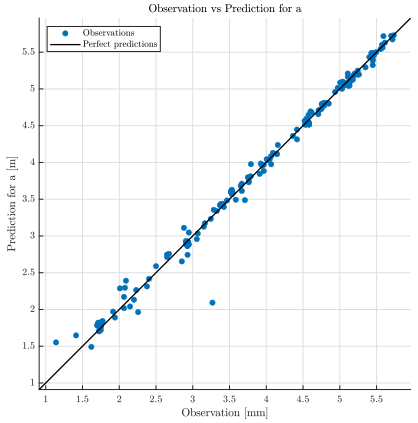

(b) Predictions for semi-major axis.

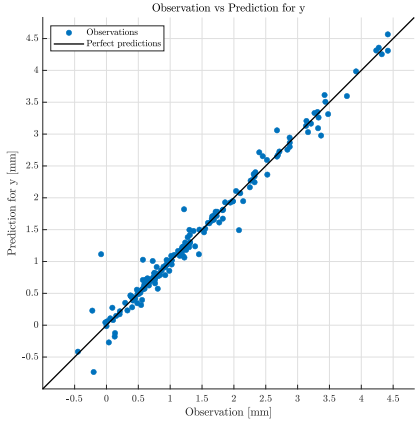

(c) Predictions for position of the center.

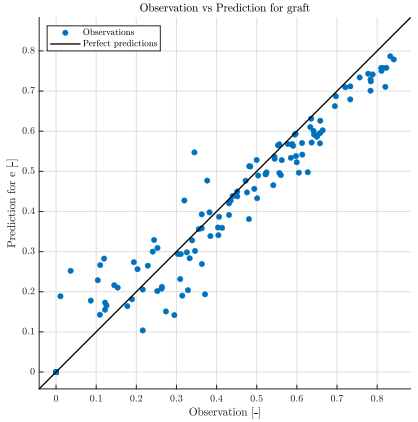

(d) Predictions for the eccentricity

Figure D.3: Actual predictions and observations versus the perfect prediction (i.e., prediction equals observation) for the outputs of interest using MATLAB's `Regression Learner`.

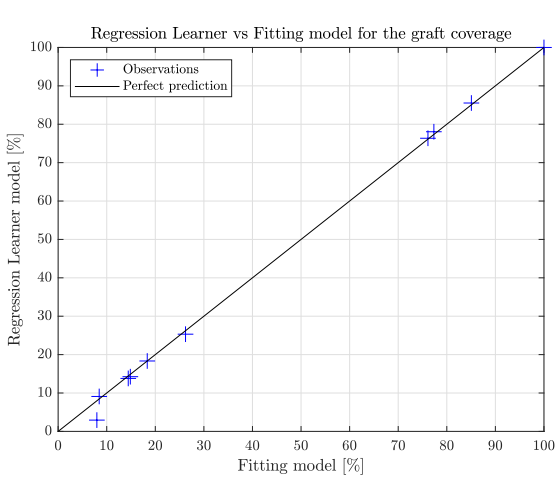

(a) Graft coverage.

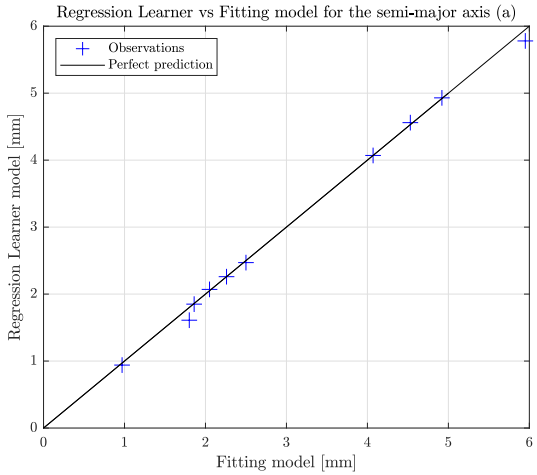

(b) Semi-major axis.

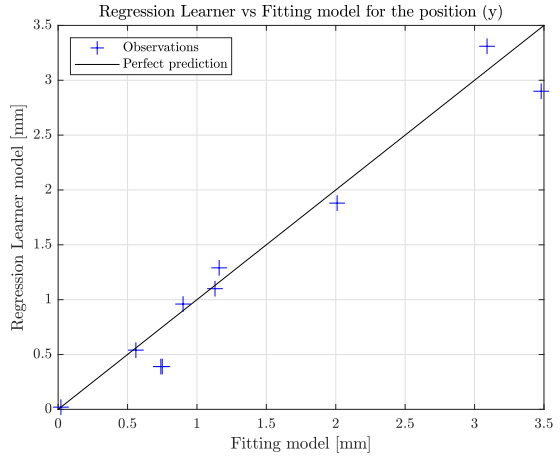

(c) Position of the center.

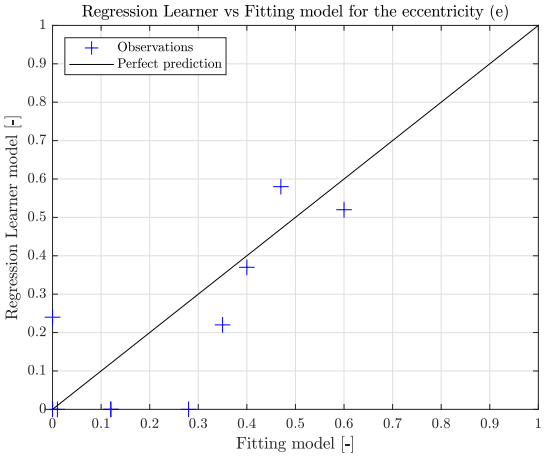

(d) Eccentricity.

Figure D.4: Comparison of the solution obtained with my fitting model and the `Regression Learner` Machine Learning model from MATLAB.

Bibliography

[1] J. O. Pralits, M. Alberti, and J. Cabreizo, "Gas-graft coverage after DMEK: A clinically validated numeric study", *Translational Vision Science and Technology*, vol. 8, no. 6, 2019, ISSN: 21642591. DOI: 10.1167/tvst.8.6.9.

[2] M. Alberti, *Air versus SF6 for Descemet's Membrane Endothelial Keratoplasty (DMEK), ClinicalTrials.gov NCT03407755*. [Online]. Available: https://clinicaltrials.gov/ct2/show/NCT03407755.

[3] Y. Kurimoto, M. Park, H. Sakaue, and T. Kondo, "Changes in the anterior chamber configuration after small-incision cataract surgery with posterior chamber intraocular lens implantation", *American Journal of Ophthalmology*, vol. 124, no. 6, 775–780, 1997. DOI: 10.1016/s0002-9394(14)71694-0.

[4] S. M. Mojon-Azzi and D. S. Mojon, "Waiting times for cataract surgery in ten European countries: An analysis using data from the SHARE survey", *British Journal of Ophthalmology*, vol. 91, no. 3, pp. 282–286, 2007, ISSN: 00071161. DOI: 10.1136/bjo.2006.098145.

[5] J. Kanellopoulos and G. Asimellis, "Clear-cornea cataract surgery: Pupil size and shape changes, along with anterior chamber volume and depth changes. a scheimpflug imaging study", *Clinical Ophthalmology*, p. 2141, 2014. DOI: 10.2147/opth.s68370.

[6] J. V. Godinho and S. I. Mian, "Update on Descemet membrane endothelial keratoplasty", *Current Opinion in Ophthalmology*, vol. 30, no. 4, pp. 271–274, 2019, ISSN: 15317021. DOI: 10.1097/ICU.0000000000000577.

[7] N. Gerber-Hollbach, J. Parker, L. Baydoun, V. S. Liarakos, L. Ham, I. Dapena, and G. R. Melles, "Preliminary outcome of hemi-Descemet membrane endothelial keratoplasty for Fuchs endothelial dystrophy", *British Journal of Ophthalmology*, vol. 100, no. 11, pp. 1564–1568, 2016, ISSN: 14682079. DOI: 10.1136/bjophthalmol-2015-307783.

[8] R. Repetto, J. O. Pralits, J. H. Siggers, and P. Soleri, "Phakic iris-fixated intraocular lens placement in the anterior chamber: Effects on aqueous flow", *Investigative Ophthalmology and Visual Science*, vol. 56, no. 5, pp. 3061–3068, 2015, ISSN: 15525783. DOI: 10.1167/iovs.14-16118.

[9] K. Kapnisis, M. V. Doormaal, and C. Ross Ethier, "Modeling aqueous humor collection from the human eye", *Journal of Biomechanics*, vol. 42, no. 15, pp. 2454–2457, 2009, ISSN: 00219290. DOI: 10.1016/j.jbiomech.2009.07.025. [Online]. Available: http://dx.doi.org/10.1016/j.jbiomech.2009.07.025.

[10] H. Von Helmholtz, *Handbuch der physiologischen Optik*, Third. University of Michigan Library, 1909.

[11] OpenCFD, *Snappyhexmesh*, 2016. [Online]. Available: https://www.openfoam.com/documentation/guides/latest/doc/guide-meshing-snappyhexmesh.html.

[12] K. Miyake, K. Maekubo, S. Miyake, A. Yamauchi, H. Futamura, P. Gravagna, and J. L. Tayot, "Measuring contact angles of the lens capsule, collagen type I and collagen type IV", *European Journal of Implant and Refractive Surgery*, vol. 6, no. 3, pp. 132–137, 1994, ISSN: 09553681. DOI: 10.1016/S0955-3681(13)80403-0.

[13] U. Spandau and H. Heinmann, *Practical Handbook for Small-Gauge Vitrectomy. A step-by-step introduction to surgical techniques*. Springer, 2012, vol. XIX.

[14] F. Feuerlock, *The vitruvian man - download free 3d model by fritz feuerlocke (@manhiac) [6c0b99c]*. [Online]. Available: https://sketchfab.com/3d-models/the-vitruvian-man-6c0b99ce8463468fbd00f304dbe7e105.

[15] S. Eduardo, *Adherence to long-term therapies: evidence for action*. World Health Organization, 2003.

[16] Christensen D. B., "Drug-taking compliance: a review and synthesis.", *Health services research*, vol. 13, no. 2, pp. 171–187, 1978.

[17] G. Savini, K. Hoffer, and M. Carbonelli, "Anterior chamber and aqueous depth measurement in pseudophakic eyes: Agreement between ultrasound biometry and scheimpflug imaging", *Journal of refractive surgery (Thorofare, N.J. : 1995)*, vol. 29, pp. 121–5, Feb. 2013. DOI: 10.3928/1081597X-20130117-07.

[18] A. Hemami, *Wind turbine technology*. Delmar, Cengage Learning, 2012.

[19] M. S. Gorovoy, "Dmek complications", *Cornea*, vol. 33, no. 1, 101–104, 2014. DOI: 10.1097/ico.0000000000000023.

[20] S. W. Smith, "Properties of Convolution", in *Digital Signal Processing*, 2003, pp. 123–140. DOI: 10.1016/b978-0-7506-7444-7/50044-3.

[21] J. T. Leek and R. D. Peng, "What is the question?", *Science*, vol. 347, no. 6228, pp. 1314–1315, 2015, ISSN: 0036-8075. DOI: 10.1126/science.aaa6146. eprint: https://science.sciencemag.org/content/347/6228/1314.full.pdf. [Online]. Available: https://science.sciencemag.org/content/347/6228/1314.

[22] G. C. Cawley and N. L. Talbot, "On over-fitting in model selection and subsequent selection bias in performance evaluation", *Journal of Machine Learning Research*, vol. 11, pp. 2079–2107, 2010, ISSN: 15324435.

[23] G. Seni and J. F. Elder, "Ensemble methods in data mining: Improving accuracy through combining predictions", *Synthesis Lectures on Data Mining and Knowledge Discovery*, vol. 2, no. 1, 1–126, 2010.

[24] C. E. Rasmussen, "Gaussian processes for machine learning", MIT Press, 2006.